ϕ- and ω- meson production at RHIC energies using the PHENIX detector

February 19, 2009

Final Report submitted to the Feinberg Graduate School of the Weizmann Institute of Science

Deepali Sharma

Supervisor: Prof. Itzhak Tserruya

Department of Particle Physics

Weizmann Institute of Science

Rehovot, Israel

Contents

List of Figures

List of Tables

Abstract

The physics aim of this thesis is the study of ϕ and ω- mesons production via the e^+e^- decay channel in $p+p$ and $d+Au$ collisions at an energy of $\sqrt{s_{NN}} = 200$ GeV using the PHENIX detector[1] at the Relativistic Heavy Ion Collider(RHIC) at BNL, USA[2]. The $p+p$ measurement are essential as they serve as a baseline for all the heavy-ion collisions such as $Cu+Cu$ and $Au+Au$. On the other hand $d+Au$ measurements are important to understand the cold nuclear matter effects. The analysis is based on the data collected by PHENIX in years 2005 ($p+p$) and 2008 ($d+Au$).

Besides the analysis part, my thesis involves a hardware part. I participated in the construction, installation and commissioning of the Hadron Blind Detector (HBD)[3] which is built as an upgrade for the PHENIX detector to enhance the low mass dilepton measurements. The HBD was installed and commissioned in the year 2007. The final detector was installed towards the end of year 2008 and is ready for the upcoming run at RHIC. In addition, I took part in the physics runs, Run5 (2005), Run6 (2006) Run7 (2007) and Run8 (2008) of the PHENIX detector at RHIC.

1 Motivation

Low Mass Vector mesons are considered to be one of the most interesting probes to study the properties of strongly interacting matter created in heavy-ion collisions. A precise knowledge of their production rates and spectral properties are important in understanding the medium properties. Due to their short lifetimes, *e.g.*, 23 fm/c for ω and 46 fm/c for ϕ, a considerable fraction of them decays inside the fireball, thus providing information about in-medium modifications of their spectral shape that could be linked to the restoration of chiral symmetry. These changes can be observed directly without any distortion through their dilepton decay modes as dileptons interact only electromagnetically and have a relatively large mean free path compared to the size of the system. These modifications could manifest themselves as changes in the spectral shapes or in the branching ratios. In particular, since $m_\phi \approx 2m_K$, even small changes in the spectral properties of ϕ or K can induce significant changes in the $\phi \rightarrow K^+K^-$ yield.

One of the most interesting findings at the RHIC is the suppression of high p_T light mesons in relativistic heavy-ion collisions, compared to the expectations from $p+p$ collisions. At high transverse momentum ($>$ 5GeV/c), the magnitude of the suppression based on the existing data converges to some universal constant of 0.2-0.3, whereas below p_T $<$ 5 GeV/c, particle exhibit different behavior. Study of the LVM provides an important input in the understanding of suppression mechanisms by looking into particles with different properties and quark content.

The PHENIX detector at RHIC is a versatile detector that has the potential to measure the LVM properties. A brief overview of the PHENIX detector follows in the next section 2. In this report, I present the work done by me about ϕ and ω mesons production measured by PHENIX via di-electrons in $p+p$ and $d+Au$ collisions at $\sqrt{s_{NN}}$ = 200 GeV using the data collected during the years 2005 and 2008. This aims at measuring the spectra and invariant cross-sections of these mesons in both systems and a comparison to the hadronic decays. These measurements serve as an important reference to study medium effects in $Au+Au$ collisions.

2 The PHENIX Detector

PHENIX, Pioneering High Energy Nuclear Interaction eXperiment is one of the four experiments associated with the heavy-ion program at the Relativistic Heavy Ion Collider(RHIC) at BNL, USA. The others are; STAR[6], PHOBOS[5] and BRAHMS[4]. It was designed specially to measure the direct probes of collisions such as leptons, photons, muons and also hadrons, using its multipurpose detectors. The set-up of the PHENIX detector can be seen in fig. 1.

The PHENIX subsystems can be categorized into four groups, beam detectors, magnets, central arms and muon arms. The beam detectors are used for triggering and event characterization. The magnets comprise a central magnet and two muon magnets, that are used to measure the momenta of charged particles. The Central arms consist of east and west arms and are used to detect electrons, photons and hadrons at midrapidity ($|\eta| < 0.35$). The two muon arms are symmetrically placed around the beam pipe(North and South) and are specialized in muon identification and tracking in the forward and backward rapidity regions ($1.2 < |\eta| < 2.4$). A brief description of the detector subsystems used in this analysis follows in the next sections.

2.1 PHENIX Beam Detectors

PHENIX uses Beam Beam counters (BBC) [7] and Zero-Degree Calorimeters (ZDC) [8, 9] to measure the global properties of a collision, such as collision vertex and collision centrality. There are two identical BBCs, each made up of 64 $\check{C}$erenkov PMTs with quartz glass radiators, placed along the beam-axis at a distance of 1.44m on the north and south side of the interaction point. The BBCs provide trigger for the collisions at the interaction point, and time and vertex information of the collisions. The BBCs provide a timing resolution of 52$\pm$4ps (rms), corresponding to a vertex resolution of 1.1 cm.

The ZDCs are small hadron calorimeters positioned at each of the four RHIC exper-

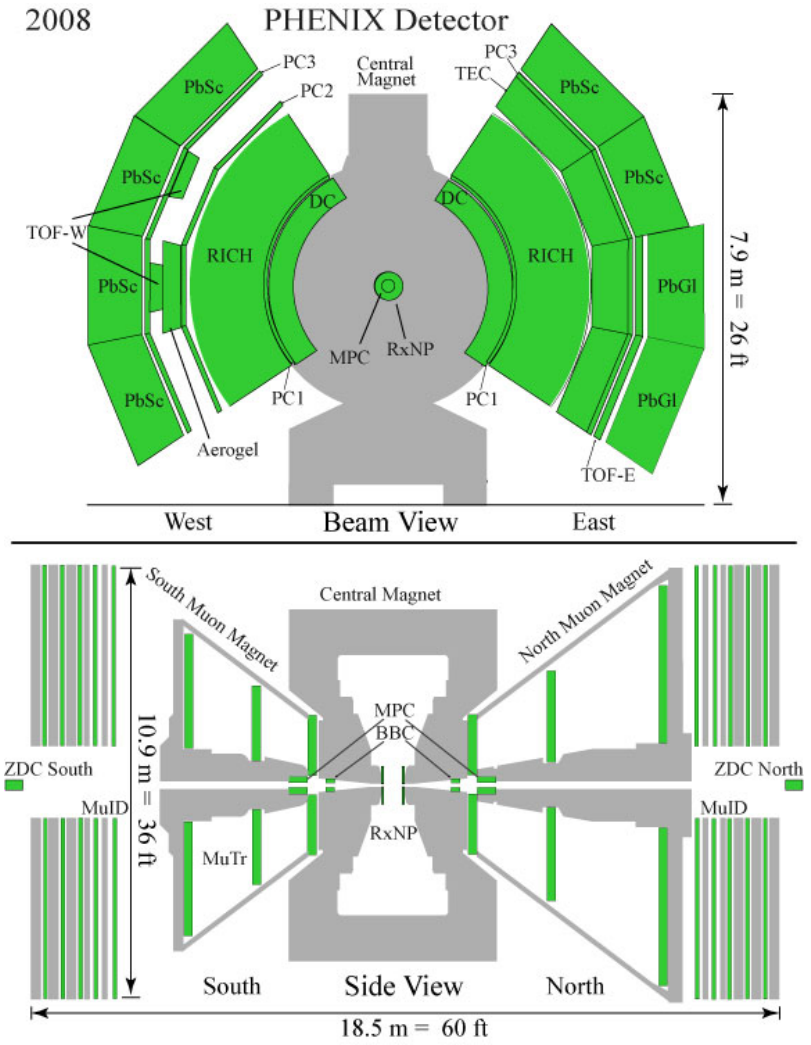

Figure 1: The PHENIX detector layout for the year 2008. The upper panel shows the beam view where two central arms and central magnets can be seen. The lower panel shows a cut away view along the beam axis, two muon arms, central magnet and muon magnets can be seen.

iments. They are placed about 18.25 m up and downstream of the beam pipe behind the beam bending magnets, so that charged particles will be deflected out of the acceptance before they can hit the ZDC. Their purpose is to measure the energy of spectator neutrons, which did not participate in the collision and thus carry a large fraction of the beam momentum. The total energy deposited by spectator neutrons in anticorrelation with the total charge deposited in the BBC is used to determine the centrality of the collision which is a measure of the impact parameter of two colliding nuclei.

2.2 PHENIX Central Arm Detectors

The two central arms consist of a variety of subsystems used for charged particle tracking, identification and momentum measurement. Each arm covers $|\eta| < 0.35$ in pseudo-rapidity and $|\varphi| = \pi/2$ in azimuth. The central arm co-ordinate system of PHENIX has its origin at the nominal interaction point, with the $\hat{z}$-axis along the beam direction pointing north, $\hat{x}$-axis pointing west and the $\hat{y}$-axis pointing upwards $\perp$ to the two other axis. A brief description of the central arm detectors used in the analysis is given in the following subsections.

2.3 Central Magnet

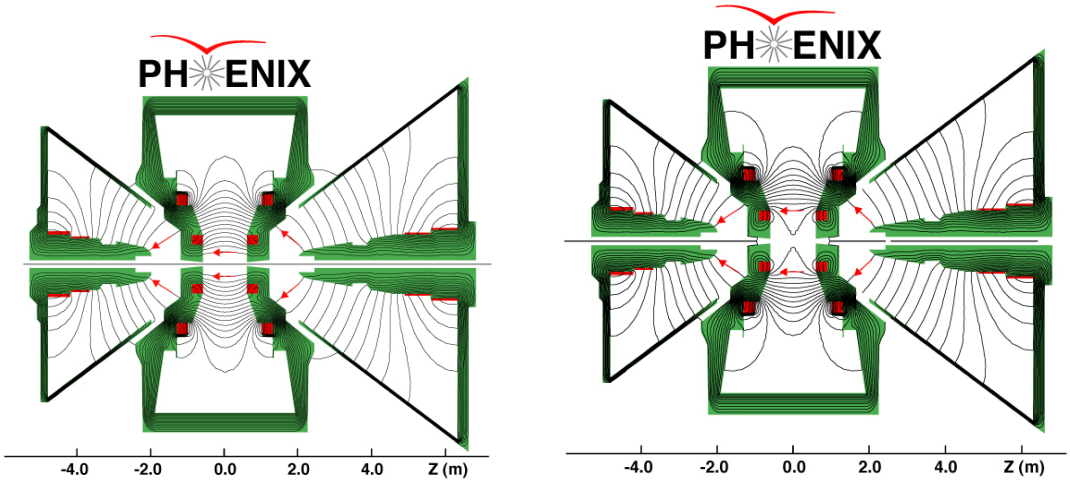

(a) (b)

Figure 2: Magnetic field lines in the PHENIX detector, for the two central magnet coils in ++(left) and +-(right) mode.

The momentum of charged particles is measured by the bending in the magnetic field provided by the Central Magnet. The central arm magnets provide an axial field along the beam axis bending the charged particles in azimuthal angle in the central-arm region, where the Drift Chambers have better resolution. Each central magnet is energized by two (inner and outer) pairs of concentric coils, that can be run independently providing several field configurations. For example, the "++"configuration (Fig. 2) has both coils pointing their fields to positive z-axis direction (or "–" to the negative z-axis direction). In the "++" configuration, the total field integral $\int B.dl$ = 1.5 Tm is achieved over the first 2 m from the interaction point, while the magnetic field in the region of the tracking devices ($R > 2$ m) is nearly zero to allow a tracking model that assumes straight tracks and to minimize smearing of $\check{C}$erenkov rings in the Ring Imaging $\check{C}$erenkov Detector. A "+-" magnetic

field configuration on the other hand leads to a cancellation of the field in the first 50 cm around the interaction region to approximately zero field integral, which is needed for Hadron Blind Detector (Section 8). For Run5 and Run8, the field configurations used were "- -" and "++" respectively.

2.4 Tracking Detectors

The Drift Chambers(DC) The main purpose of drift chambers [10] is to measure charged particle trajectories in the $r-\phi$ direction to determine the transverse momentum (p_T) of each particle. Each of the two PHENIX Drift Chambers (east or west) cover 90°in ϕ, has a radial sensitive region from 2.02 m to 2.46 m, and covers 1.8 m along the beam direction as an active area. They are operated with a mixture of 50% Argon and 50% Ethane. Each DC volume is constructed with a cylindrical titanium frame, divided in 20 equal sectors covering 4.5°in ϕ. Each sector in turn is divided into four drift cells with six units of different wire types in the following order: X1, U1, V1, X2, U2, V2. The X1 and X2 wires are aligned parallel to the beam pipe for $r-\phi$ measurements. The U and V wires are tilted by a small $\approx \pm 6°$stereo angle relative to the X wires, to allow for full three-dimensional track reconstruction.

The tracking in PHENIX is based on the assumption that tracks have a straight line trajectory inside the Drift Chamber volume. Track reconstruction is performed using a *Combinatorial Hough Transform* technique [11, 12]. In this technique, the drift chamber hits are mapped pair-wise into a 2-dimensional space defined by the coordinates ϕ_{DC} and α. The angle ϕ_{DC} is the azimuthal angle of the track at its intersection with the DC reference radius R as shown in Fig. 3, and α is the inclination angle between the track candidate and an infinite momentum ($i.e$ straight) track at angle ϕ_{DC}. α is proportional to the inverse of the transverse momentum and its sign depends on the charge of the particle. The momentum resolution is given by:

$$\delta p/p = \sigma_{m.s} \oplus \sigma_{DC}.p(GeV/c) \tag{1}$$

where $\sigma_{m.s}$ is the contribution due to mutiple scattering and σ_{DC} is the intrinsic momentum resolution of the DC. The resolution measured in Run3 was about $\delta p/p$ = 0.7%$\oplus$ 1.1%p. With the increased field strength in Run4, the measured value of σ_{DC} improved to $\sim$0.76%.

The Pad Chambers(PC) The Pad Chamber system [13] is the second subsystem used for particle tracking. It is used to determine three dimensional spatial positions which are used for momentum determination in the z direction. There are three sets of Pad

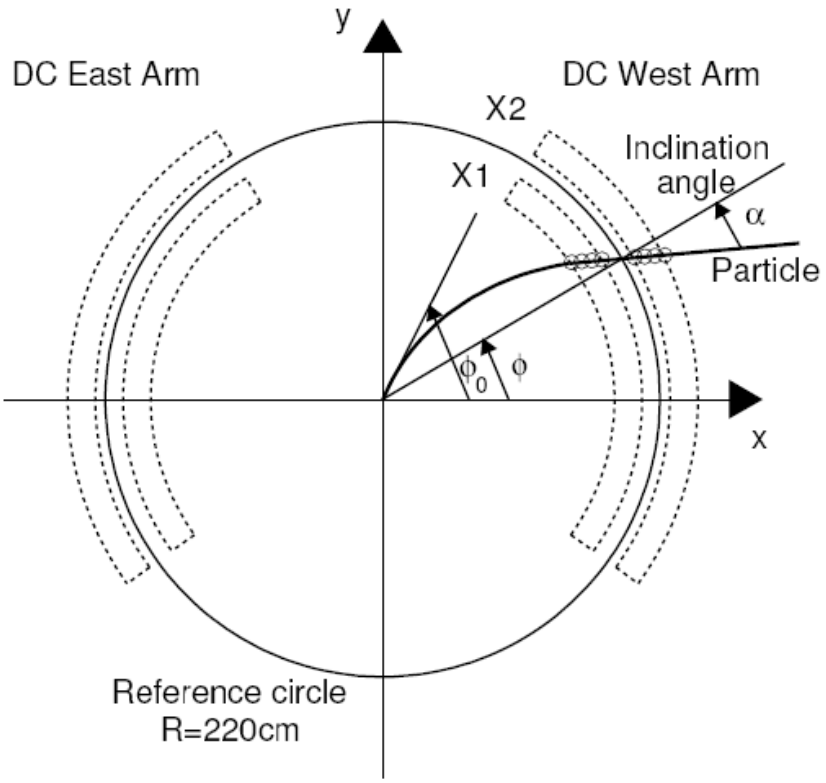

Figure 3: Illustration of the Hough transform parameters for Drift Chamber track reconstruction. The dashed lines show the drift chamber active volume. The circles represent drift chamber hits along the particle trajectory.

Chambers instrumented in PHENIX, called PC1, PC2 and PC3. The PC1 is the innermost chamber, occupying 2.47-2.52m in the radial direction from the interaction point and located between the DC and the RICH detectors in both east and west arms. The PC2 layer exists only in the west arm and is placed behind the RICH at $r = 4.15 - 4.21m$. The PC3 is placed in front of the electromagnetic calorimeter and occupies $r = 4.91 - 4.98m$. The PC1 is essential for the 3D momentum determination by providing the z-coordinate at the exit of the DC. The DC and PC1 information are combined to get straight line trajectories outside the magnetic field and PC2 and PC3 are needed to resolve ambiguities in the outer detectors where about 30% of the particles striking the EMCal are produced by either secondary interaction or decays outside the aperture of DC and PC1.

The Pad Chambers are multi-wire proportional chambers, each one made up of a single plane of wires in a gas volume surrounded by two cathode planes. One cathode is finely segmented into an array of pixels. The charge induced on a number of pixels when a charged particle starts an avalanche on an anode wire is read out to determine precise

$x,\ y,\ z$ position of the track.

2.5 Electron Identification Detectors

The main detectors used for electron identification are RICH and EMCal.

Electromagnetic Calorimeter(EMCal) The Electromagnetic Calorimeter(EMCal) is used for the determination of the energy and spatial position of electrons and photons produced in beam collisions. The EMCal consists of two subsystems: six sectors of lead scintillator (PbSc) detectors and two sectors of lead-glass (PbGl) detectors (lower half of the east arm), with each sector covering 22.5°in azimuth and $\Delta\eta = \pm$ 0.35 in pseudo-rapidity. The PbSc is a shashlik type sampling calorimeter consisting of 15552 individual towers, with each tower made up of 66 sampling cells made of alternating tiles of Pb and scintillator. The PbGl is comprised of 9216 modules and each module has a lead glass crystal of 40mm $\times$ 40mm $\times$ 40mm. The complete description of PbSc and PbGl can be found in [14]. Both set of detectors provide excellent timing, good position and energy resolution. The PbSc has an excellent timing resolution of about 100 ps for electrons and photons nearly independent of the incident energy, with an energy resolution (σ_E/E) of about 8.1%/$\sqrt{(E(GeV))}\oplus$2.1%. The PbGl on the other hand, has an excellent energy resolution of 5.9%/$\sqrt{(E(GeV))}\oplus$0.8%.

Ring Imaging $\check{C}$erekov Detector(RICH) Each of the two central arms is equipped with a Ring Imaging $\check{C}$erenkov detector [15]. The RICH detector is one of the primary devices to identify electrons among the large number of charged hadrons. Charged particles moving faster than the speed of light in the gas emit $\check{C}$erenkov photons in the RICH vessel. Each RICH detector has a volume of 40 m^3 and is filled with CO_2 as radiator gas that has a refractive index n= 1.00410 at 20°C and 1 atm [16]. This corresponds to a threshold velocity β_t = 1/n = 0.99590168 and a γ - factor of γ_t=1/$\sqrt{1-\beta^2}$ = 34.932. leading to a $\check{C}$erenkov threshold of $p_T = me\gamma\beta$ = 18 MeV/c for electrons ($m_\pi = 0.511$ MeV/c^2) and 4.9 GeV/c for pions ($m_\pi = 139.57$ MeV/c^2). Below the π-threshold, RICH provides a hadron rejection of 10^4 to 1. The emitted photons are reflected and focussed by two intersecting spherical mirrors onto a plane of phototube array.

2.6 Trigger

The collision-event rate is usually higher than the recording ability and so a triggering system is needed that can select potentially interesting events and provide sufficient rejection of uninteresting events to reduce the data rate to a level which can be handled by

the PHENIX data acquisition system [17]. The trigger for an inelastic collision is usually given by BBC and forms the basic PHENIX Level-1 trigger. For $p+p$ and $d+Au$ collisions, it requires a coincidence between the north and south sides of the BBC, with at least one hit on each side and accepts the events if the BBC vertex is within 30 cm of the nominal interaction vertex. These cuts are performed online by BBC Level-1 trigger. Since this trigger is efficient for most interaction processes, it is referred to as *Minimum Bias* (MB) trigger.

$$MB \equiv (BBC \geq 1) \cap (|z_{vertex}| < 30\ cm) \tag{2}$$

The MB trigger accepts 88.5 $\pm$4 % of all d+Au collisions that satisfy the vertex condition, and 54.5 $\pm$ 6% of $p+p$ collisions. The total inelastic cross-section for $p+p$ collisions is σ^{pp}_{BBC} = 42.2 $\pm$ 1.9 mb. Simulations, and data collected without requiring the BBC trigger, indicate that the triggered events include 79 $\pm$ 2 % of events with particles in the central arms acceptance. This number coincides with the fraction of non-diffractive events triggered by the BBC. For $d+Au$ collisions, the total inelastic cross-section is σ^{dAu}_{BBC} = 2260 $\pm$ 100 mb. As for $p+p$ collisions, there is a trigger bias, but it is much smaller in $d+Au$ (94 $\pm$ 2 %).

To select and enhance rare events containing e.g. electrons or photons, PHENIX uses some specialized triggers. One of these is an EMCal RICH trigger (*ERT*) that relies on the information from the RICH and EMCal detectors and allows us to identify electrons and collect rare electron and di-electron events. The acceptance coverage of each of the EMCal and RICH detectors is divided into 16 trigger segments. Each segment consists of 9(PbSc)/16(PbGl) and 16 RICH trigger tiles. Each trigger tile consists of 144 EMCal towers (20 RICH phototubes). EMCal has two different methods, 2×2 tower sum and 4×4 tower sum, to sum the energy of towers. The energy threshold value (E^{th}_{ERT}) of EMCal for the hit definition can be changed. If there is a hit tile defined by 2×2 sum in the EMCal part, ERTLL1_2x2 is issued. The ERT trigger (ERTLL1_E) then requires a geometrical coincidence of this particular EMCal tile with the corresponding RICH tile (4×5 PMT's) determined using a look-up table, which is defined on the basis of single-electron Monte Carlo simulation. The efficiency of the ERT trigger is discussed in Section 4.3.

A brief description of the PHENIX subsystems is summarized in the table 1.

3 Data Analysis

This section presents the details of analysis of ϕ and ω - mesons in $p+p$ and $d+Au$ collisions at $\sqrt{s_{NN}}$ =200 GeV. The analysis of both data sets follows a similar procedure, so

Subsystem	$\Delta\eta$	$\Delta\phi$	Specifications
Magnet: central	$\pm$0.35	360°	Upto 1.15T· m
muon south	-1.1 to -2.2	360°	0.72 T·m for η=2
muon nouth	1.1 to 2.4	360°	0.72 T·m for η=2
Beam-beam counters (BBC)	$\pm$ 3.1 to 3.9	360°	Start timing, fast vertex
Zero-degree Calorimeter (ZDC)	$\pm$2 mrad	360°	Minimum-bias trigger
Drift Chambers (DC)	$\pm$0.35	2×90°	Good momentum and mass resolution $\Delta m/m$ = 0.4% at m = $1GeV$
Pad Chambers (PC)	$\pm$0.35	2×90°	Pattern recoginition tracking in non-bend direction
Ring-Imaging $\check{C}$erenkov Detector (RICH)	$\pm$0.35	2×90°	Electron identification
Time-of-flight (TOF)	$\pm$0.35	45°	hadron ID,$\sigma <$ 100 ps
PbSc EMCal	$\pm$0.35	90°+ 45°	Electron/Photon ID
PBGl EMCal	$\pm$0.35	45°	Good $e^{\pm}/\pi^{\pm}$ separation at $p > 1$ GeV/c by EM shower and $p <$0.35 GeV/c by TOF. $K^{\pm}/\pi^{\pm}$ separation up to 2.4GeV/c by TOF
μ-tracker: south	-1.15 to -2.25	360°	μ tracking
north	1.15 to 2.44	360°	μ tracking
μ-ID: south	-1.15 to -2.25	360°	μ/hadron separation
nouth	1.15 to 2.44	360°	μ/hadron separation

Table 1: Summary of PHENIX subsystems

they are discussed in parallel, highlighting the differences where they exist. The analysis procedure can be divided into the following steps.

- Event selection that includes vertex determination and trigger selection.
- Track selection and electron identification.
- Pair analysis that involves estimating the background and signal extraction.
- Monte Carlo simulations to account for acceptance, reconstruction and trigger effects.

3.1 Data Set and Event Selection

The analysis is based on the data sets collected during the years 2005 ($p + p$) and 2008 ($d + Au$) at $\sqrt{s_{NN}}$ = 200 GeV and will be referred to as Run5 and Run8 in the text.

Both analyses were done for two types of event samples: minimum bias events, a reference sample of events which are selected by the minimum bias trigger (MB)(Sec. 2.6), and electron triggered events (ERT)(Sec. 2.6) that contain at least one electron. Events collected over a certain period of time (usually 30 minutes up to 1 hour) represent individual runs, wherein the global settings of the data acquisition, e.g. prescale factors of the triggers, and of the detectors remain unchanged.

Events with the collision vertex far from the center of the detector (z_{vtx} = 0 cm) have a higher probability to interact with the nose cones of the central magnet leading to additional conversion electron background. As seen in Fig. 4(a), the vertex distribution is centered around z_{vtx} = 0 cm, and has a FWHM of $\approx$ 30 cm, but a clear increase in the number of electrons per event can be seen outside $-30 \leq z_{vtx} \leq 28$ due to material of the central magnets in Fig. 4(b). Thus a vertex cut of $-30cm \leq z_{vtx} \leq 28cm$ is applied in $p+p$ analysis and $|z_{vtx}| \leq 30$ cm fin the $d+Au$ analysis. The bbc vertex distribution and the corresponding number of electrons per event for $d+Au$ data can also be seen in Fig. 4(c) and 4(d).

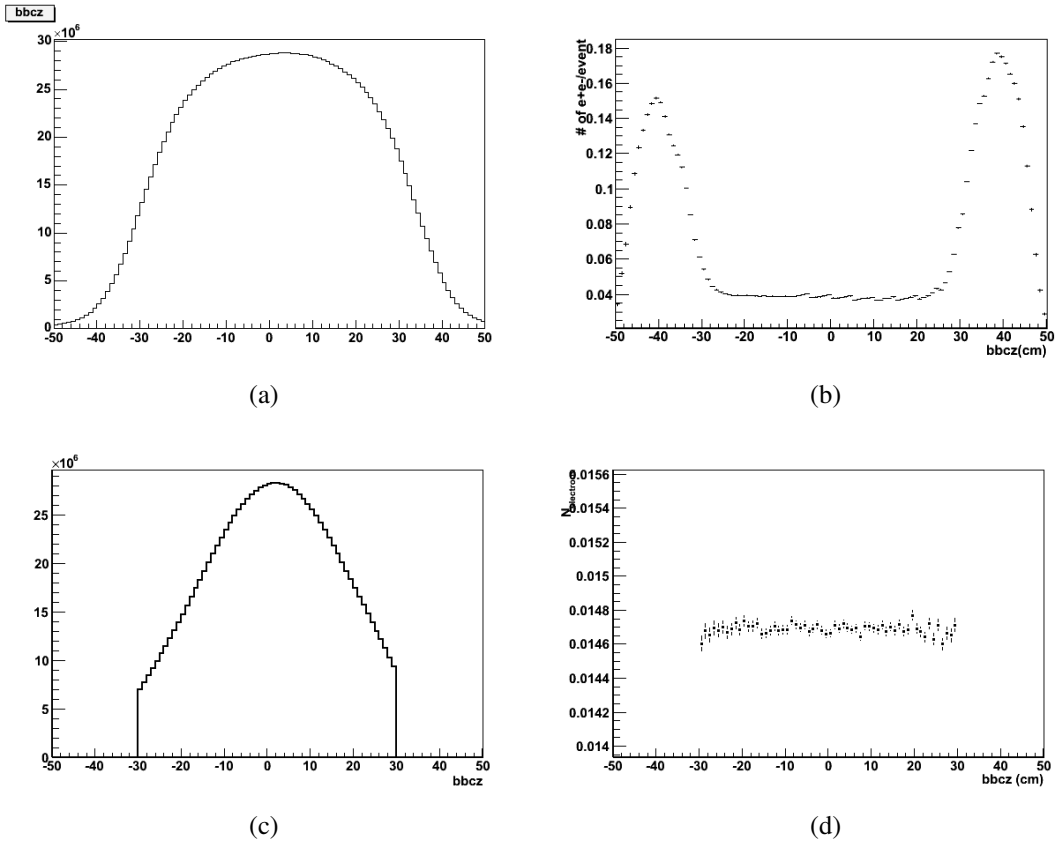

(a) (b)

(c) (d)

Figure 4: bbcz vertex distribution(a) and number of $(e^+ + e^-)$ per event as a function of bbcz (b) for $p+p$ and $d+Au$ (c) and (d)

Due to the limited bandwidth of the data acquisition, usually only a fraction of all

minimum bias events is recorded. This fraction is determined by a scale down factor, specified at the beginning of a run for each trigger and is subject to change depending on the beam conditions. These scale down factors are recorded in the database and need to be considered when determining the total luminosity recorded. The number of sampled minimum bias events corresponding to the ERT data set is calculated from the sample of minimum bias events as follows:

$$N_{MB}^{sampled} = \sum_{run} N_{MB} \cdot f_{scale\_down\_factor}^{run} \cdot N_{ERT}^{MB}/N_{MB}^{ERT} \tag{3}$$

where N_{MB} is the number of events recorded with the MB trigger in a particular run, with a scale down factor $f_{scale\_down\_factor}$. $N_{ERT}^{MB}/N_{MB}^{ERT}$ serves as a correction for the cases when during the data reconstruction, some file segment[1] of either the MB or ERT sample is lost. In this case the number of ERT triggered events in the ERT sample (N_{ERT}^{MB}) is not equal to the number of MB triggered events in the ERT sample (N_{MB}^{ERT}). This ratio as a function of run number can be seen in Fig. 5(a) and a 1D projection can be seen in Fig. 5(b). As can be seen the ratio is equal to one except for 5 runs, which are corrected by this ratio. The total number of analyzed events is summarized in the Table 2.

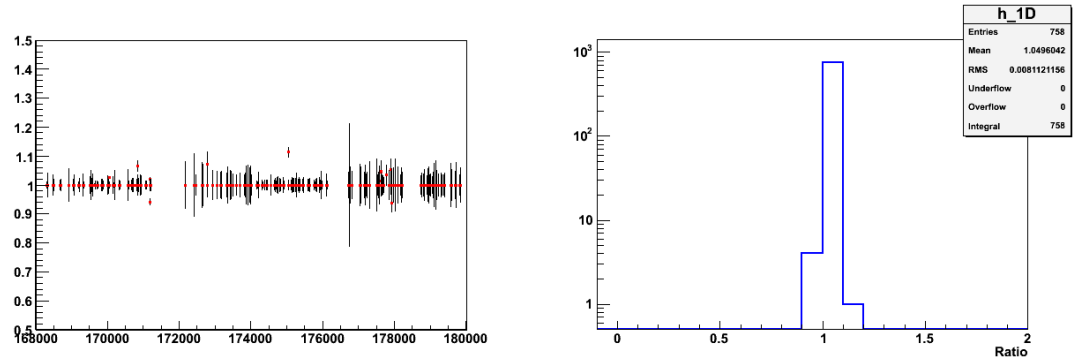

(a) $N_{ERT}^{MB}/N_{MB}^{ERT}$ as a function of run number

(b) $N_{ERT}^{MB}/N_{MB}^{ERT}$

Figure 5: Ratio of triggered events in the ERT and MB samples

3.1.1 Run Selection

The electron yield per event as a function of run number can fluctuate due to certain external factors, such as detector dead areas, unstable DAQ conditions, or extra material in the detector. To simplify the analysis we select a set of runs with similar features and this can be represented by the electron yield per event. Fig. 6 shows the number of

[1] A Run is divided into certain segments to keep the size of the output files low and allow parallel processing during the offline production

	Run 5 $p+p$	Run 8 $d+Au$
Vertex cut	-28 $\leq$ z_{vtx} $\leq$ 30	$\lvert z_{vtx} \rvert$ $\leq$ 30
Data sample	ERT and MB	ERT and MB
ERT threshold	400 MeV	600 MeV
Sampled MB events	53.01 B	51.8 B
ERT events	261 M	1.4 B

Table 2: Data samples and event statistics

electrons and positrons per event based on the eID cuts described in Table. 4, using the MB data sample. For $p+p$ ($d+Au$) analysis, runs with N_{e^+}/evt and N_{e^-}/evt lying between 0.0004 (0.004) and 0.001 (0.0062) were selected.

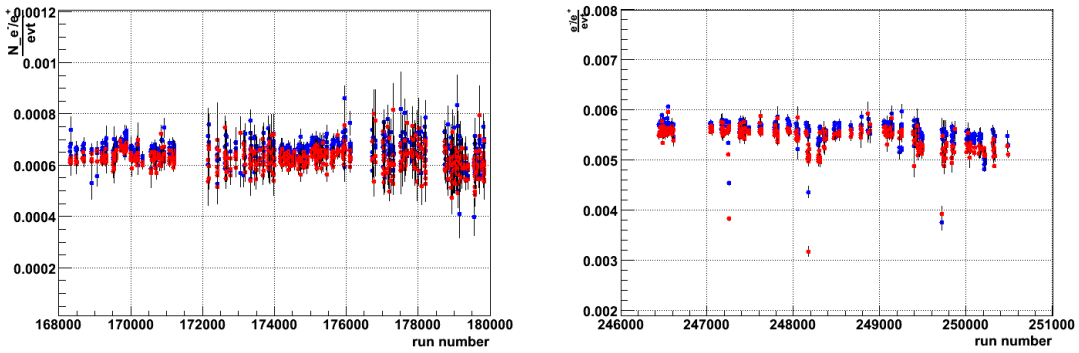

(a) $p+p$ (b) $d+Au$

Figure 6: Number of e^+ (blue) and e^- (red) per event for $p+p$ as a function of run number for $p+p$ collisions (left) and $d+Au$ collisions

3.2 Track selection and electron identification

3.2.1 Track quality

The track reconstruction algorithm associates hit information of X (X1 or X2 or both) and UV wires in the DC to the information from the PC1 hits and the collison vertex, z_{vtx} determined by BBC. This information is combined in a 6-bit variable, **quality,** Q_{track} defined using the following binary pattern:

$$Q_{track} = A \times 2^0 + B \times 2^1 + C \times 2^2 + D \times 2^3 + E \times 2^4 + F \times 2^5 \tag{4}$$

where A, B, C, D, E, F are quality bits defined as follows:

- A = 1 if X1 plane is used.
- B = 1 if X2 plane is used.

Comment	A	B	C	D	E	F	Quality, Q_{track}
$PC1^{found}_{unique}$ & UV^{found}_{unique}	1	0	1	1	1	1	61
	0	1	1	1	1	1	62
	1	1	1	1	1	1	63
$PC1^{found}_{unique}$ & no UV	1	0	0	0	1	1	49
	0	1	0	0	1	1	50
	1	1	0	0	1	1	51
$PC1^{found}_{ambiguous}$ & UV^{found}_{unique}	1	0	1	1	1	0	29
	0	1	1	1	1	0	30
	1	1	1	1	1	0	31
$PC1^{found}_{ambiguous}$ & UV^{found}	1	0	1	0	1	0	21
	0	1	1	0	1	0	22
	1	1	1	0	1	0	23
$PC1^{found}_{ambiguous}$ & no UV	1	0	0	0	1	0	17
	0	1	0	0	1	0	18
	1	1	0	0	1	0	19

Table 3: Summary of DC track quality

- C = 1 if there are hits in UV plane.
- D = 1 if there are unique hits in UV plane.
- E = 1 if there are hits in PC1.
- F = 1 if there are unique hits in PC1.

otherwise bits are set to 0. This leads to set of patterns summarized in Table: 3. The highest quality that a track can have is 63, $i.e.$, it is reconstructed based on hits in the X1 and X2 planes, with a unique PC1 and UV hit. The $p+p$ analysis used all track qualities to have more statistics. For $d+Au$ analysis, the tracks with quality 63 or 31 or 51 were used. The track quality distributions for Run5 and Run8 are shown in Fig. 7.

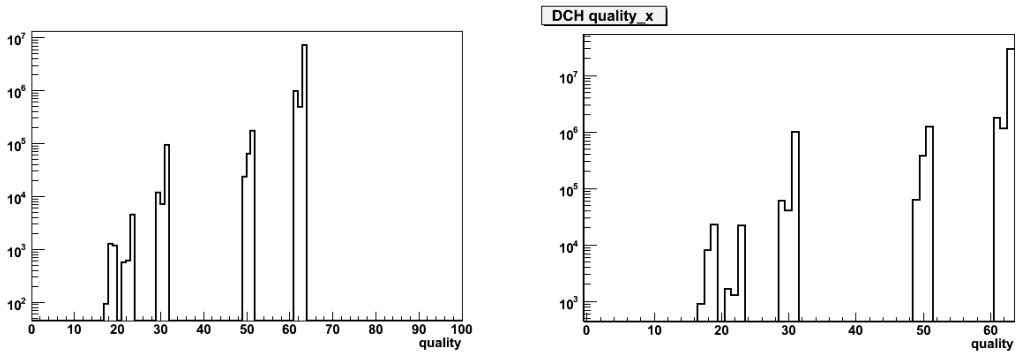

(a) $p+p$ (b) $d+Au$

Figure 7: Track quality distributions in Run 5 (left) and Run 8 (right)

3.2.2 electron Identification

The electron identification is achieved using RICH and EMCal as described in Section: 2.5. The electrons are primarily identified using the RICH detector. An electron in the RICH produces an average of 10 $\check{C}$erenkov electrons within $cos(\theta) = 1/(\eta\beta)$, that get focused to rings in the PMT plane with an asymptotic radius of $\approx$ 5.4 cm. The tracks reconstructed using the Drift and Pad Chambers are projected onto the PMT plane and the number of fired PMTs ($n0$) associated to this projection point are counted.

$n0$ = the number of fired phototubes between $3.4 \leq r^i_{cor} \leq 8.4$ cm

where a fired phototube in RICH is required to have a signal greater than 0.2 photo-electron and r^i_{cor} is the distance between the center of phototube i and the track projection. For both analyses, a value of $n0 \geq 2$ is used. The pulse height measured in each PMT gives the number of photo-electrons ($N_{p.e}(i)$) associated to it. Using the position of the fired phototubes and ($N_{p.e}(i)$), a weighted position of the ring center is calculated. The distance between the ring center and the track projection is called **disp** (displacement). For $d + Au$ analysis, we use a value of disp $\leq$ 5 cm. The $n0$ and $disp$ distributions are shown in Fig. 8 and 9 respectively.

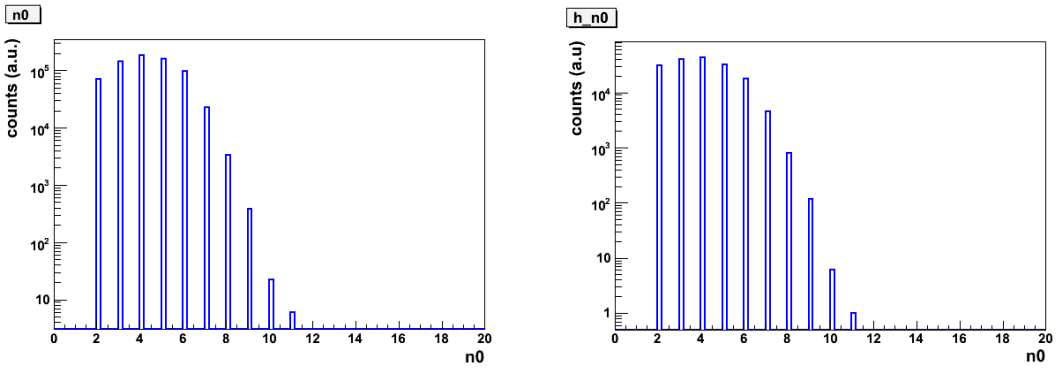

(a) $p + p$ (b) $d + Au$

Figure 8: n0 distribution

Further electron identification relies on the energy measured in the EMCal. Since the electron mass ($m_{e^+e^-}$ = 511 KeV/c^2) is negligible compared to its momentum $p >$ 200 MeV/c and all its energy is deposited in the EMCal, the ratio of the energy (**E**) measured by the EMCal and the total momentum (**p**) measured by the DC is about 1 ($E = \sqrt{p^2 + m^2} \simeq p$). Fig. 10 shows the **E/p** distribution in $p + p$ and $d + Au$ collisions for all charged particles (black), tracks after requiring an $n0 > 1$ cut for eID (blue) and also the contribution from accidental association with RICH. Electrons from

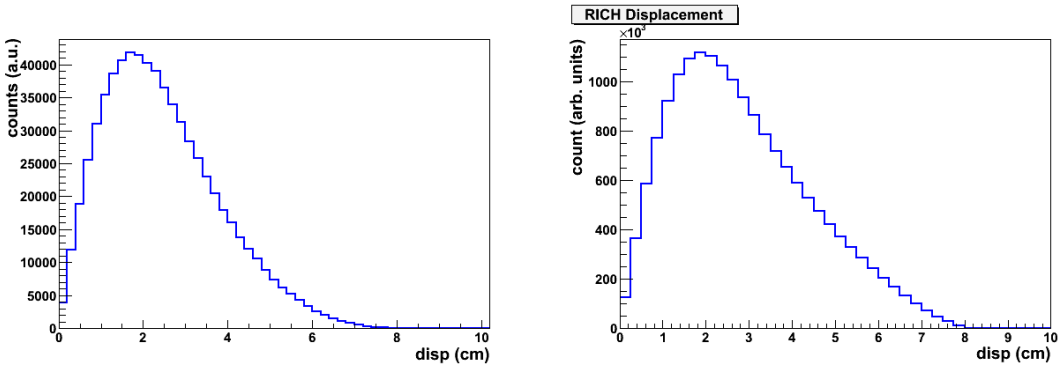

(a) $p+p$ (b) $d+Au$

Figure 9: displacement distribution

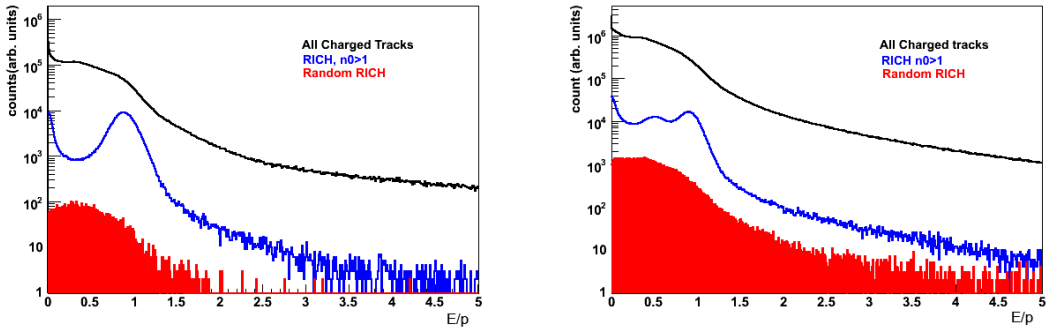

(a) $p+p$ (b) $d+Au$

Figure 10: E/p distribution in $p+p$ (left) and $d+Au$ (right), for all charged tracks (black), tracks after applying the RICH cuts (blue) and contribution of hadrons randomly associated to hits in RICH (red).

off-vertex decays or late conversions have a mis-reconstructed momentum as the tracking algorithm assumes all tracks to originate from the collision vertex. Off-vertex decays traverse less magnetic field integral and are therefore bent less, which results in a larger reconstructed momentum and an $E/p < 1$.

Distances between the projection point of a reconstructed track at the EMCal and the hit position (the centroid of the electromagnetic shower) are expressed in the $\hat{z}$ and φ, **emcdze** (cm) and **emcd**φ (radians) respectively. The variables **E/p, emcd**φ and **emcdz** depend on the total momentum, the electric charge and EMCal sector due to the residual field. An example of raw distributions for these three variables for electrons for one EMCal sector E0 and p_T bin 0.35-0.45 GeV/c, is shown in Fig. 11. For the analysis, these variables are normalized to a convenient standard normal distribution having a mean 0 and σ 1. The normalized variables are called **dep, emcsdphi_e** and **emcsdz_e**. This is done by fitting the raw distributions of each of these variables to a Gaussian function for each EMCal sector and momentum bin, separately for electrons and positrons. The extracted

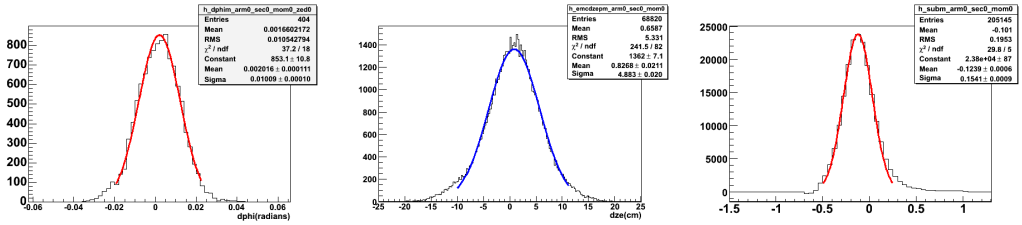

(a) dφ-distribution (b) dze-distribution (c) E/p distribution

Figure 11: Track matching along the z- and φ- co-ordinates and E/p distribution for sector E0 and momentum bin 0.35 - 0.45 GeV/c, fitted with gaussian function.

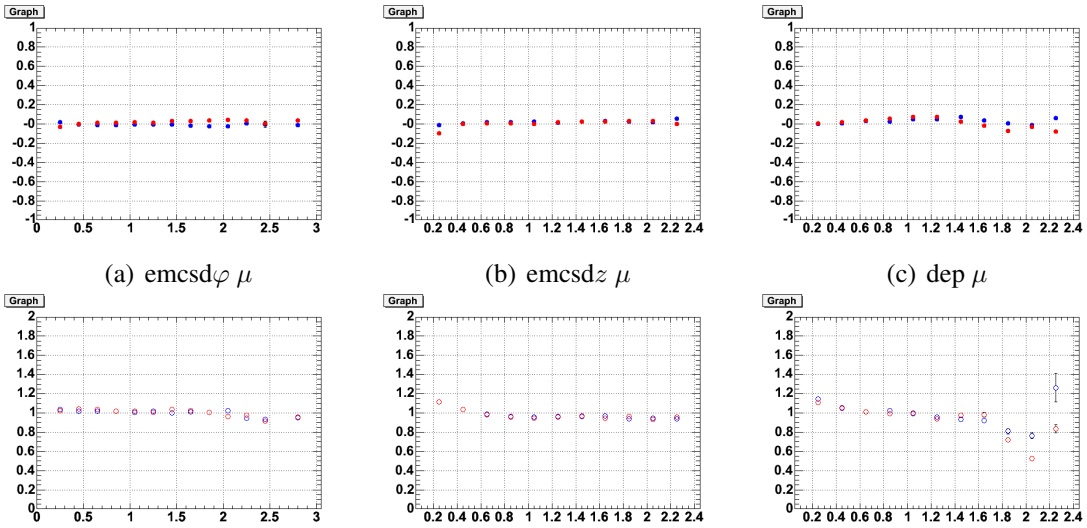

(a) emcsdφ μ (b) emcsd$z$ μ (c) dep μ

(d) emcsdφ σ (e) emcsd$z$ σ (f) dep σ

Figure 12: Mean (upper panels) and Sigma (lower panels) of track matching along z- and φ- co-ordinates and dep distributions as a function of p_T for one EMCal sector for the east arm for $p+p$ collisions. Blue and Red points represents e^+ and e^- respectively

centroid and sigma from the fits are then used to derive these reduced variables.

$$dep = \frac{ecore/p - \langle ecore/p \rangle}{\sigma(ecore/p)}; emcsdz\_e = \frac{emcdz - \langle emcdz \rangle}{\sigma(emcdz)}; emcsdphi\_e = \frac{emcd\varphi - \langle emcd\varphi \rangle}{\sigma(emcd\varphi)}; \quad (5)$$

An example of normalized means and sigmas for **dep, emcsdphi_e** and **emcsdz_e** is shown in Fig. 12 and Fig. 13 for $p+p$ and $d+Au$ respectively. In $p+p$ ($d+Au$), the reconstructed tracks were required to have a 3.5 (3) σ matching to the associated EMCal clusters. A summary of the eID cuts used in two analysis is shown in the Table. 4.

3.3 Pair Analysis

All the identified electrons in a given event based on the cuts described in the Section. 3.2.2 are combined into pairs to generate the invariant mass, $m_{e^+e^-}$ distribution.

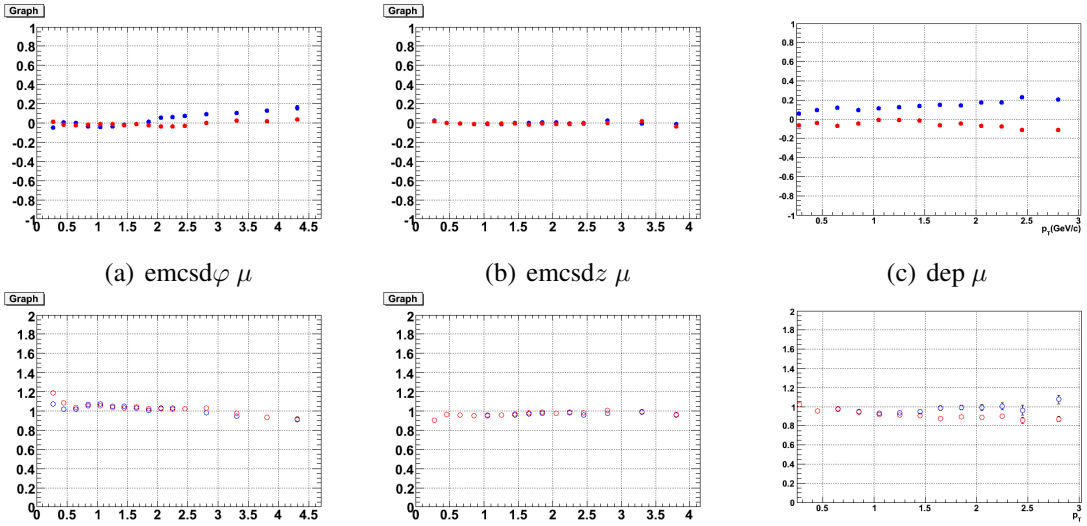

(a) emcsdφ μ (b) emcsd$z$ μ (c) dep μ

(d) emcsdφ σ (e) emcsd$z$ σ (f) dep σ

Figure 13: Mean (upper panels) and Sigma (lower panels) of track matching along z- and φ- co-ordinates and dep distributions as a function of p_T for one EMCal sector for the east arm for $d + Au$ collisions. Blue and Red points represents e^+ and e^- respectively

	Run 5 $p + p$	Run 8 $d + Au$
quality cut	All	63 || 31 || 51
n0	> 1	> 1
disp	No cut	$\leq$5
dep	$>$ -2	$>$ -2
$\sqrt{emcsd\varphi^2 + emcsdz^2}$	$\leq$ 3.5	$\leq$ 3

Table 4: Electron identification cuts for $p + p$ and $d + Au$.

It is checked that at least one of the tracks in each pair is associated to a hit of the ERT trigger. The Invariant mass of the e^+e^- pair is calculated as follows:

$$m^2_{e^+e^-} = (p_{e^+} + p_{e^-})^2 = (E_{e^+} + E_{e^-})^2 - (\overrightarrow{p}_{e^+} + \overrightarrow{p}_{e^-})^2 \quad (6)$$

with $E_{e^+(e^-)} = \sqrt{\overrightarrow{p}_{e^+(e^-)}{}^2 + m_e{}^2}$, m_e = 511 keV/c^2, and the 3- momentum vector $\overrightarrow{p}_{e^+(e^-)}$ as measured with the drift chamber. Fig. 14 shows the mass spectra from ERT events for $p + p$ and $d + Au$ collisions. By construction the mass spectra contains both the signal and an inherent combinatorial background of uncorrelated pairs that originates mainly from unrecognized π^0 Dalitz decays and γ-conversions. The size and shape of the background is estimated by a fitting procedure, the details of which follows in the next section.

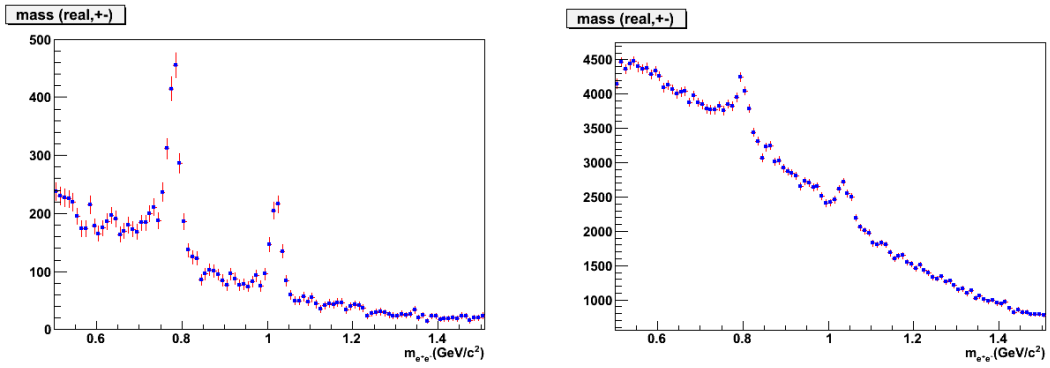

(a) $p + p$ (b) $d + Au$

Figure 14: Invariant mass spectra distribution for $p + p$ and $d + Au$

3.3.1 Raw yield extraction

For the $p + p$ analysis, we chose 9 p_T bins; $0 \leq p_T < 0.25$, $0.25 \leq p_T < 0.5$, $0.5 \leq p_T < 0.75$, $0.75 \leq p_T < 1.0$, $1.0 \leq p_T < 1.25$, $1.25 \leq p_T < 1.5$, $1.5 \leq p_T < 2.0$, $2.0 \leq p_T < 3.0$, $3.0 \leq p_T < 4.0$ GeV/c and 5 p_T bins for the $d + Au$ analysis; $0 \leq p_T < 0.5$, $0.5 \leq p_T < 1.0$, $1.0 \leq p_T < 1.5$, $1.5 \leq p_T < 2.0$, $2.0 \leq p_T < 3.0$, $3.0 \leq p_T < 5.0$. In order to extract the ϕ-yield, the spectrum in each p_T bin is fitted with a relativistic Breit-Wigner function convoluted with a Gaussian function for the experimental mass resolution and a polynome of 2^{nd} degree for the background. The relativistic Breit-Wigner parameterization is given by:

$$Y(m) \sim \frac{m.m_\phi.\Gamma_\phi}{(m^2 - m_\phi^2)^2 + (m_\phi.\Gamma_\phi)^2} \tag{7}$$

where the centroid m_ϕ and the full width Γ_ϕ are fixed to the PDG values. The experimental mass resolution in each p_T bin is allowed to vary within $\pm 10\%$ with respect to the value obtained from zero-width simulation of ϕ-mesons as discussed later in Section. 4.2. The yield is then determined by summing up the bins in a 3σ-window around the ϕ peak and subtracting the polynomial background. The spectra along with the fits for each p_T bin for ϕ meson are shown in Fig. 15.

The ω-meson yield was extracted following a similar procedure but adding a second relativistic Breit-Wigner function to account for the contribution of ρ-meson beneath the ω peak. The production ratio of ρ to ω meson was assumed to be 1 and so in the fit their ratio is given by the ratio of the branching ratios to e^+e^- $i.e.$ 1.53. The fits to ω peaks for various p_T bins can be seen in Fig. 16. The examples for the ω and ϕ spectra for certain bins in $d + Au$ collisions are shown in the Fig. 17. The raw yield extracted in the various p_T bins is summarized in the Tables. 5 ($p + p$) and 6.

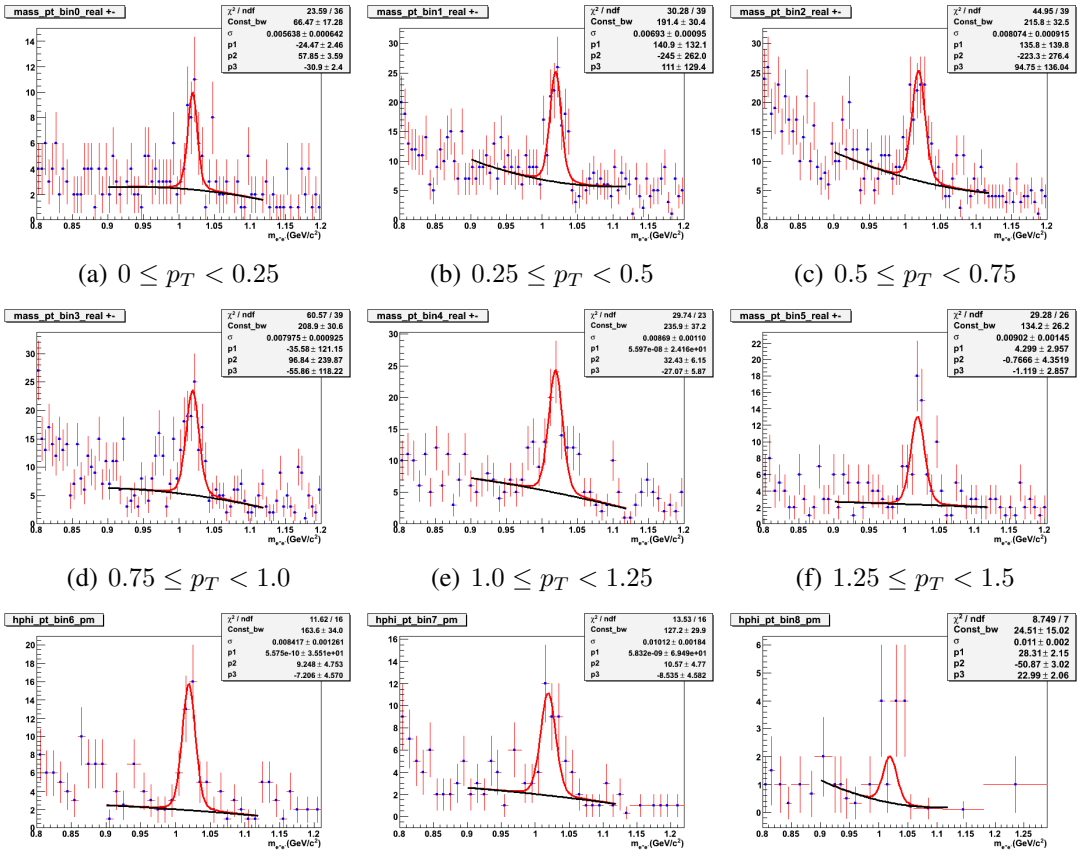

(a) $0 \leq p_T < 0.25$ (b) $0.25 \leq p_T < 0.5$ (c) $0.5 \leq p_T < 0.75$

(d) $0.75 \leq p_T < 1.0$ (e) $1.0 \leq p_T < 1.25$ (f) $1.25 \leq p_T < 1.5$

(g) $1.5 \leq p_T < 2.0$ (h) $2.0 \leq p_T < 3.0$ (i) $3.0 \leq p_T < 4.0$

Figure 15: Invariant e^+e^- mass spectrum of the ϕ meson in different p_T bins together with the fit described in the text.

p_T	0-0.25	0.25-0.5	0.5-0.75	0.75-1.0	1.0-1.25	1.25-1.5	1.5-2.0	2.0-3.0	3.0-4.0
ω	16.1(7.7)	106.1(19.2)	231.2(25.2)	187.3(21.3)	147.3(16)	89.6(11.9)	75.7(12.3)	51.9(10.2)	12.6(4.8)
ϕ	30.6(7.8)	93.5(12.1)	96.2(15.4)	98.2(13.9)	66.4(11.4)	49.9(9.3)	34.2(7.3)	30.5(7.3)	11.9(3.9)

Table 5: Raw yield of ϕ and ω in different p_T bins in $p + p$. The statistical errors are shown in parenthesis

4 Monte Carlo Simulation

The measured raw yields of resonances need to be corrected for detector acceptance, reconstruction efficiency (ε_{reco}), electron identification efficiency (ε_{eID}) and trigger efficiency (ε_{ERT}). Additionally, one needs to take into account that the detector performance is not uniform over time. The primary tool to correct for all these effects is the single particle Monte Carlo and GEANT-based "PHENIX Integrated Simulation Application" (PISA), which allows to construct simulated particles using the same analysis software as for the real data. PISA utilizes the set of characteristics (detector materials and geometry, dead and hot channel maps, gains, noise levels etc) that describe the performance of each subsystem during a selected reference period of time for each run.

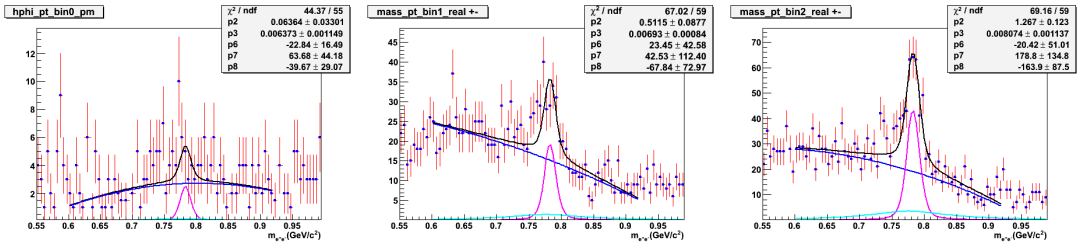

(a) $0 \leq p_T < 0.25$ (b) $0.25 \leq p_T < 0.5$ (c) $0.5 \leq p_T < 0.75$

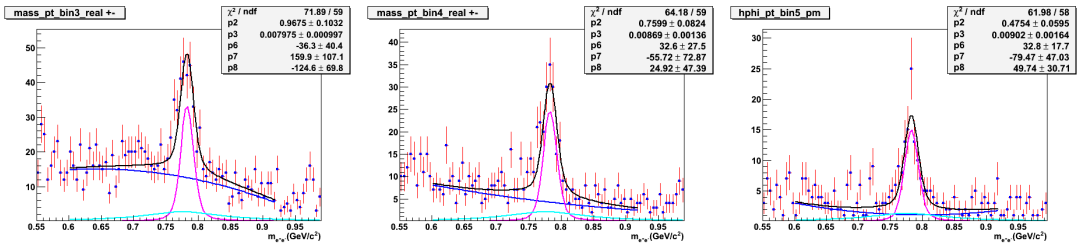

(d) $0.75 \leq p_T < 1.0$ (e) $1.0 \leq p_T < 1.25$ (f) $1.25 \leq p_T < 1.5$

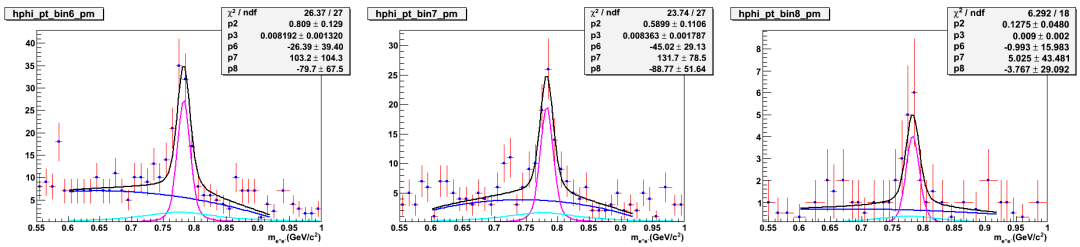

(g) $1.5 \leq p_T < 2.0$ (h) $2.0 \leq p_T < 3.0$ (i) $3.0 \leq p_T < 4.0$

Figure 16: Invariant e^+e^- mass spectrum of the ω meson in different p_T bins together with the fit described in the text.

p_T	0-0.5	0.5-1.0	1.0-1.5	1.5-2.0	2.0-3.0	3.0-5.0
ω	117.4(56.7)	496.3(114.2)	590.1(92.7)	471.7(57).1	445.3(48.7)	204.3(30)
ϕ	127.1(45.9)	284.1(87.6)	418.2(80.5)	184.1(47.7)	310.4(40.1)	150.7(22.2)

Table 6: Raw yield of ϕ and ω in different p_T bins in $d + Au$. The statistical errors are shown in parenthesis

4.1 Acceptance and Reconstruction Efficiency

The general strategy to derive this efficiency is described below.

- use the single particle generator *EXODUS* that was developed within PHENIX to generate a sample of ϕ and ω mesons with the following input specifications:
  - flat vertex distribution within $\mid z \mid < 30$ cm.
  - flat rapidity distribution within $|y| \leq 0.5$ and uniform in ϕ: $0 \leq \phi \leq 2\pi$.
  - exponential transverse momentum distribution,

$$dN/dp_T = p_T exp(-\frac{m_T}{T}),$$

where T is the inverse slope equal to 366 MeV for ϕ meson, whereas for ω a flat p_T distribution was used.

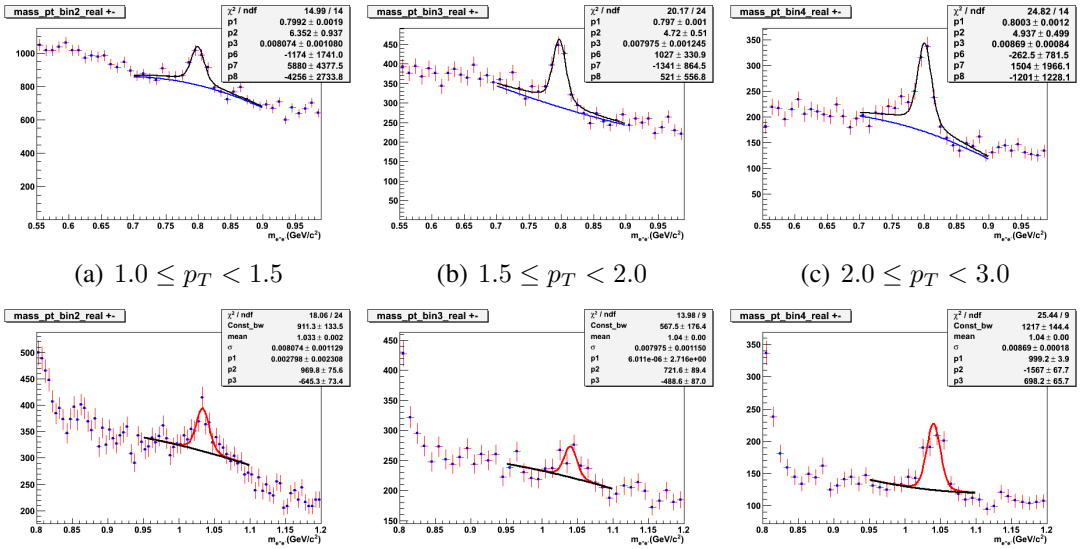

(a) $1.0 \leq p_T < 1.5$ (b) $1.5 \leq p_T < 2.0$ (c) $2.0 \leq p_T < 3.0$

(d) $1.0 \leq p_T < 1.5$ (e) $1.5 \leq p_T < 2.0$ (f) $2.0 \leq p_T < 3.0$

Figure 17: Invariant e^+e^- mass spectrum of the ω (upper panels) and ϕ- meson (lower panels) for few p_T bins together with the fits in $d + Au$ collisions

The generated events are then processed through PISA and PHENIX event reconstruction chain and the resulting output is analyzed using the same analysis chain as that for real data. The ratio of the number of generated $\phi(\omega)$ mesons to the number of accepted and reconstructed $\phi(\omega)$ mesons in each p_T bin gives the correction factors CF(p_T) = $N^{gen}(p_T)/N^{rec}(p_T)$. The measured raw spectrum is multiplied by CF(p_T) to obtain the p_T spectra corrected for acceptance and reconstruction efficiencies. The correction funcrions for ϕ and ω can be seen in Fig. 24.

4.2 Zero width MC

To get the detector resolution (σ) for each p_T bin, used in the fitting function for the raw yield extraction in the real data and also for determining correction function, we did a simulation in which the ϕ meson was generated in *EXODUS* with a zero width instead of its natural width. All other parameters of the simulation were the same as described in Section 4.1. The reconstructed ϕ-mesons for each p_T bin were fit to a Gaussian function to extract the experimental mass resolution. Table. 7 lists the σ values obtained for the bins used in this analysis. Also shown in the table are the σ values extracted from regular simulation and real data where σ's in the fit were allowed to vary within $\pm$ 10% around the zero-width values.

p_T[GeV/c]	0-0.25	0.25-0.5	0.5-0.75	0.75-1.0	1.0-1.25	1.25-1.5	1.5-2	2-3	3-4
zero-width simulation									
σ[MeV/c]	5.8	6.3	7.3	7.3	7.9	8.2	8.8	9.2	10.0
ϕ-meson Simulation									
σ[MeV/c]	5.2	5.8	6.6	6.8	7.1	7.6	7.8	8.5	9.3
Real data									
σ[MeV/c]	5.6(0.6)	6.9(1)	8.1(1)	8(0.9)	8.7(1.1)	9.0(1.5)	8.4(1.3)	10.1(1.8)	11(2)
ω-meson Simulation									
σ[MeV/c]	5.4	5.9	6.7	6.7	7.2	7.4	7.8	8.3	9.0
Real data									
σ[MeV/c]	6.4(1.2)	6.9(0.8)	8.1(1.1)	8(1)	8.7(1.4)	9(1.6)	8.2(1.3)	8.4(1.8)	9(2)

Table 7: Experimental mass resolution for different p_T bins obtained from zero-width simulations. Also listed are the σ values obtained from real data and regular simulation for ϕ and ω.

4.3 ERT Efficiency

The analysis of real data required that at least one electron in each pair is associated with a hit in the ERT trigger. This results in a bias in the pair analysis and hence needs to be corrected for. The trigger efficiency of single electrons can be determined in two ways. The first method makes use of the MB dataset only, since the Level-1 trigger decision is also recorded in MB data. Only those events are selected in which an ERT trigger is fired. However sometimes the ERT could be fired due to $e.g.$ a photon in an EMCal supermodule and noise in a RICH supermodule. This random benefit is eliminated by making sure that the electron and fired ERT trigger bits are in the matched supermodule in both the RICH and EMCal based on a look-up table (Sec. 2.6). From these selected events, we build a p_T spectrum of electron candidates $dN^{\pm}_{MB\&\&ERT}/dp^{\pm}_T$ $i.e.$, identified using the electron identification cuts. Fig. 18 shows the p_T spectra of all the electron candidates in MB events $dN^{\pm}_{MB}/dp^{\pm}_T$ (blue), ERT events (green) and after removing the random benefits (red).

The trigger efficiency is then given by the ratio of the two distributions (red and blue) as in Eq. 8. The trigger efficiency is determined individually for each EMCal sector as can be seen in Figs. 19.

$$\varepsilon_{ERT} = \frac{dN^{\pm}_{MB\&\&ERT}/dp^{\pm}_T}{dN^{\pm}_{MB}/dp^{\pm}_T} \tag{8}$$

The second method uses the ERT data set to build the ERT triggered p_T spectrum of electrons. This is then compared to the p_T spectrum from MB dataset, corrected by the scale down factor and representing the same set of data sample as used for ERT. The ERT

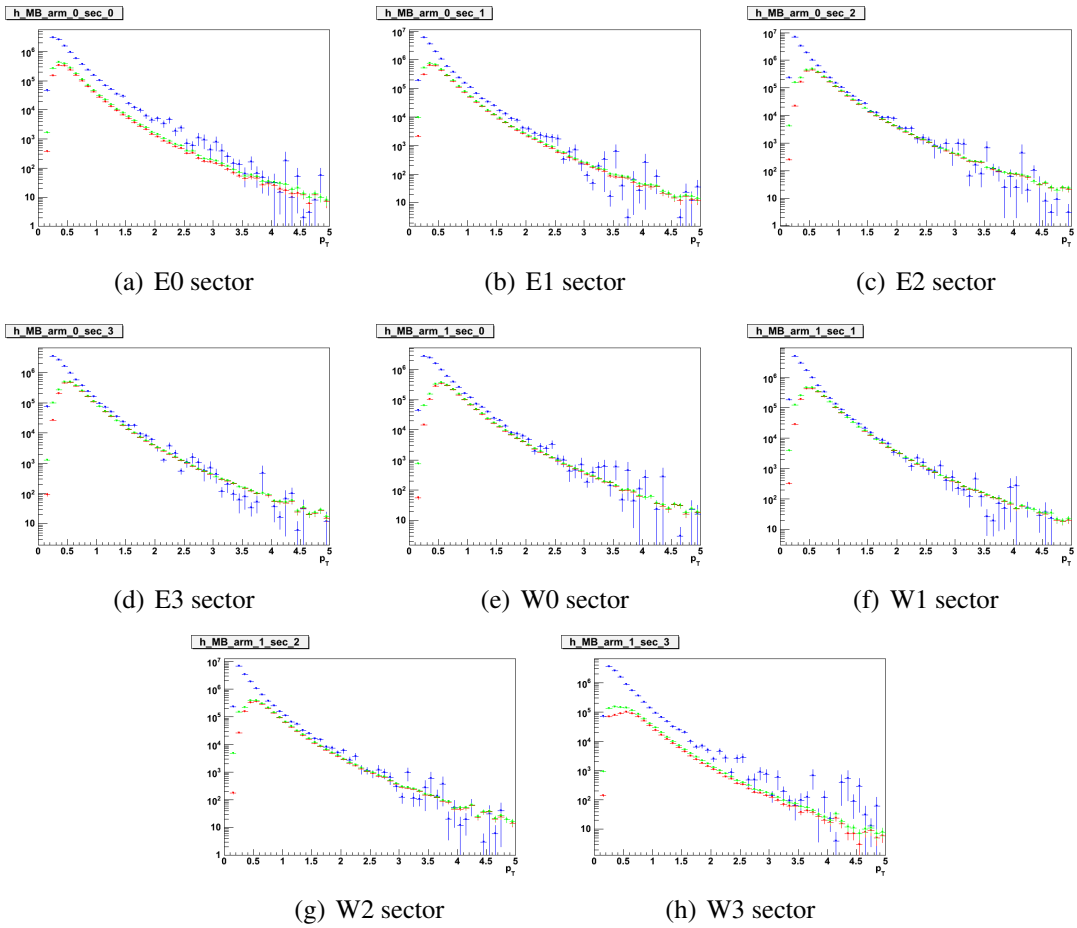

(a) E0 sector (b) E1 sector (c) E2 sector

(d) E3 sector (e) W0 sector (f) W1 sector

(g) W2 sector (h) W3 sector

Figure 18: MB and ERT single electron spectra p_T spectra for different EMCal sectors. The blue lines represent the MB electrons selected using eID cuts, the green is for those for which the ERT trigger was fired and red corresponds to those electrons after random benefit was removed.

efficiency obtained using either method gives similar results.

The plateau value of each EMCal sector is different due to the variation in the number of active trigger tiles. The trigger efficiencies are then fit to a Fermi function

$$f(p_T) = \frac{\varepsilon_0}{(e^{-}(p_T - p_0)/k) + 1} \tag{9}$$

with ε_0, p_0 and k being the free parameters. The parameters of the fit thus obtained for each EMCal sector are used in the simulations to emulate the ϕ or ω trigger efficiency. Both electron and positron of each reconstructed ϕ (ω) meson are examined for the trigger condition. This is done as follows:

- the electron and the positron are assigned a weight, w, randomly generated with a flat distribution between 0 and 1.
- The ϕ (ω) satisfies the ERT trigger if either the electron or the positron satisfies

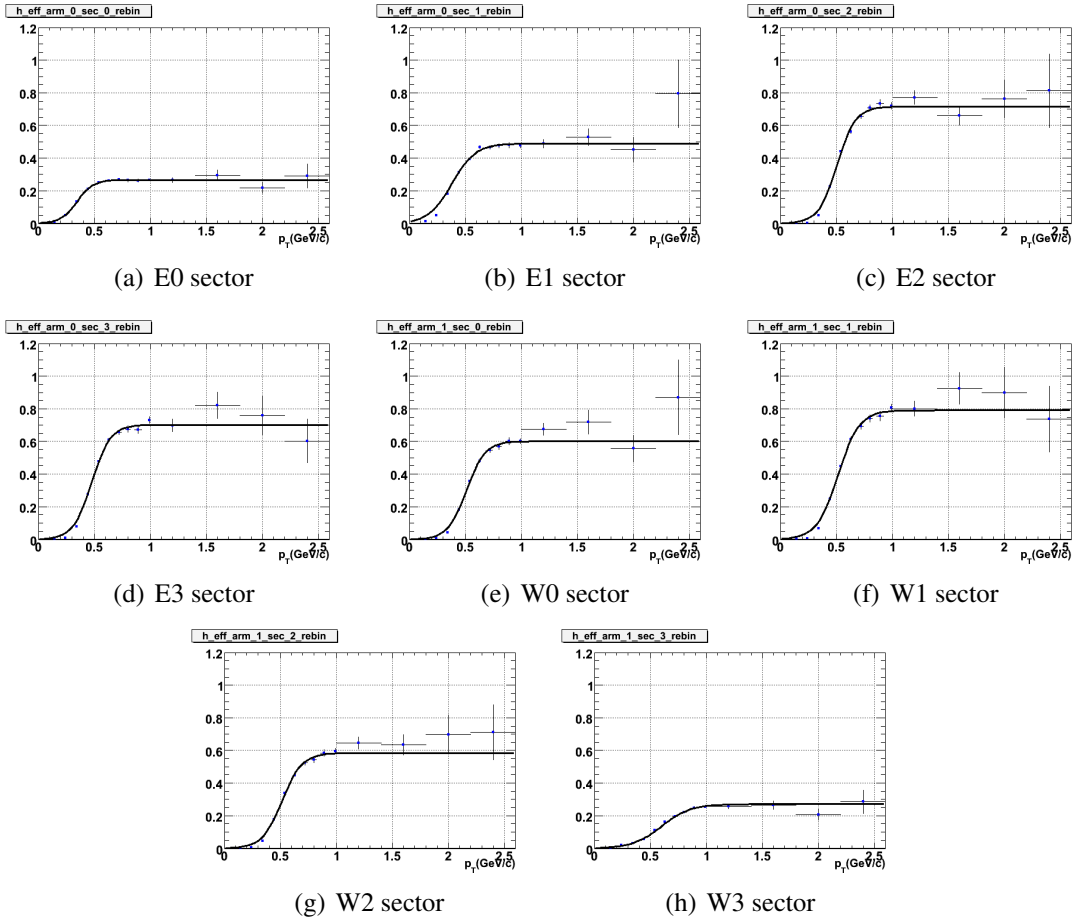

(a) E0 sector (b) E1 sector (c) E2 sector

(d) E3 sector (e) W0 sector (f) W1 sector

(g) W2 sector (h) W3 sector

Figure 19: ERT efficiency for single electrons in each EMCal sector in $p + p$ collisions

the trigger condition $w > \varepsilon_{ERT}$, where ε_{ERT} is the ERT efficiency for the given momentum of the electron or positron.

The $\phi(\omega)$ trigger efficiency is then obtained by dividing the number of $\phi(\omega)$ surviving the ERT trigger to the total number of $\phi(\omega)$ without emulating the trigger. Figs. 20 and 21 shows the pair trigger efficiency for ϕ (a) and ω (b) determined using the above mentioned procedure in $p + p$ and $d + Au$ collisions. These efficiencies are then fitted to a Fermi function and the parameterized curve is used to calculate the trigger efficiency correction in the final invariant cross-section determination.

4.4 eID Efficiency

Slight differences in the distributions of the eID parameters in real data and simulation can lead to a different fraction of signal loss in real data and simulation and hence needs to be corrected. Absolute electron identification efficiency is determined from data using a special set of runs that were taken with an additional converter material introduced into

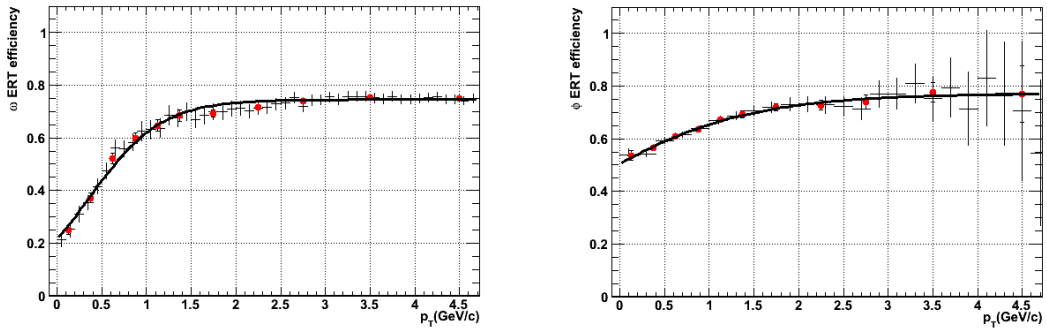

(a) ω ERT efficiency (b) ϕ ERT efficiency

Figure 20: ERT (pair) efficiency for ω and ϕ fitted to a fermi function for $p+p$ collisions

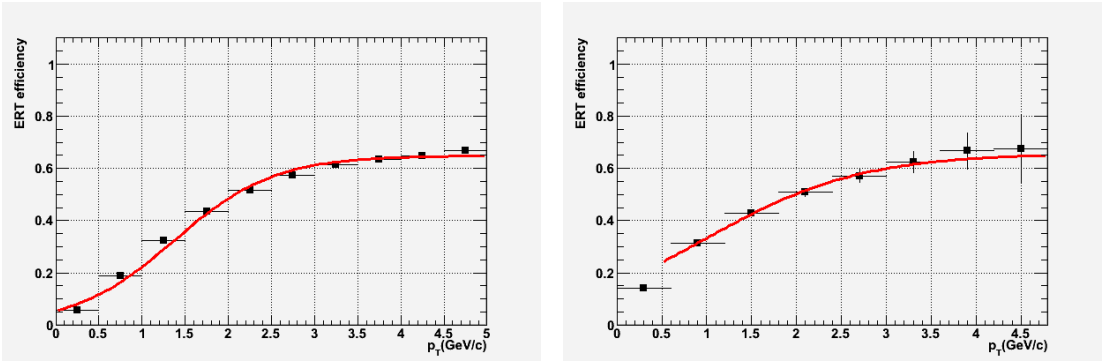

(a) ω ERT efficiency (b) ϕ ERT efficiency

Figure 21: ERT (pair) efficiency for ω and ϕ fitted to a fermi function for $d+Au$ collisions for the data sample corresponding to an ERT threshold of 600 MeV

PHENIX around the beam pipe. The basic idea is to reconstruct the photons that get converted in this material giving us a pure electron sample to study the electron identification efficiency. The reconstructed invariant mass spectrum of e^+e^- pairs produces a peak at $\sim$ 20 MeV/c^2. This is due to the fact that the PHENIX reconstruction algorithm assumes all tracks to come from the collision vertex, and therefore electrons and positrons produced at off-vertex are reconstructed with wrong momenta, giving the conversion pairs a fake invariant mass proportional to the radial distance between the photon conversion point and the collision vertex. The electron identification efficiency is determined by comparing the number of found converted photons for two cases. In the first case, strong eID cuts are applied to only one track in the $+-$ pair, and no eID cuts are applied to the second track. In the second case, the eID cuts used in the analysis are applied to the second track. The ratio of these two numbers gives the absolute electron identification efficiency. Examples of conversion photon peaks for two cases can be seen in Fig. 22 for one p_T bin. The same procedure is applied to simulation where we count the ϕ signal for the two cases. The

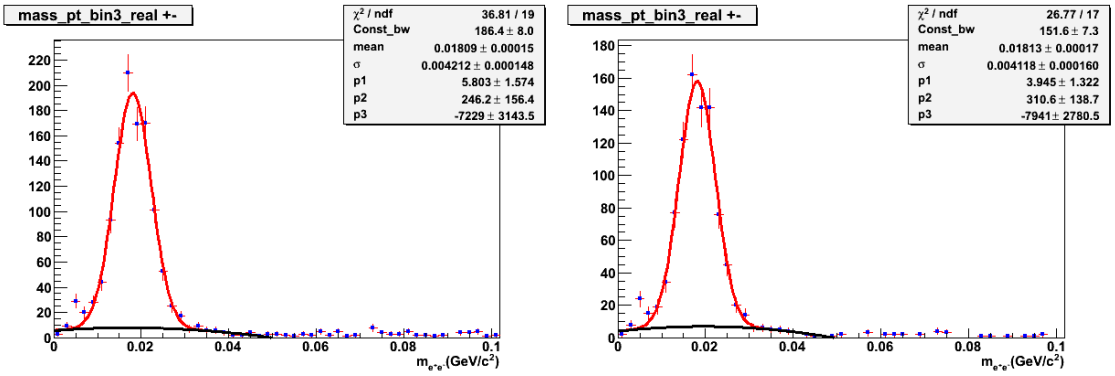

Figure 22: The left panel shows the photon conversion spectra, with strong eID cuts on the first leg and the right panel represents the same when the analysis eID cuts are applied to the second leg

two curves obtained for simulation and data, fitted with a fermi function are shown in Fig. 23(a). The ratio (simulation/data) as shown in Fig. 23(b), is then fit to another fermi function and is used to correct the simulation results.

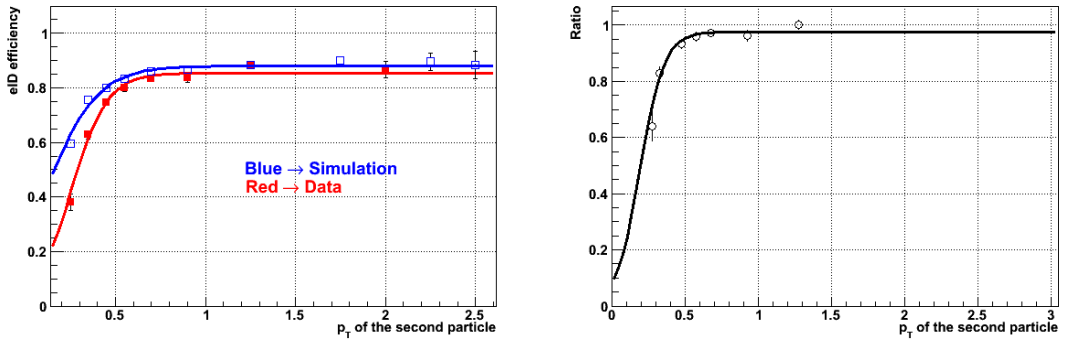

Figure 23: left panel shows eID efficiency curves for simulation (Blue) and data (Red), right panel shows a fermi function fit to the to the ratio(simulation/data)

The final correction function for ϕ (ω) including eID efficiency, is obtained by dividing the generated ϕ (ω) to the reconstructed ones and is shown in Fig. 24.

4.5 Run-by-Run Corrections

The analysis is based on data collected over a large period of time and uses several subsystems needed for the tracking and the electron identification. The performance of different subsystems can change over time which leads to variations in the yield. This run-by-run variation can be corrected by monitoring the average number of inclusive electrons per event for each run i and normalizing it to the reference run that was used in the simulations for reconstruction. This is defined as below:

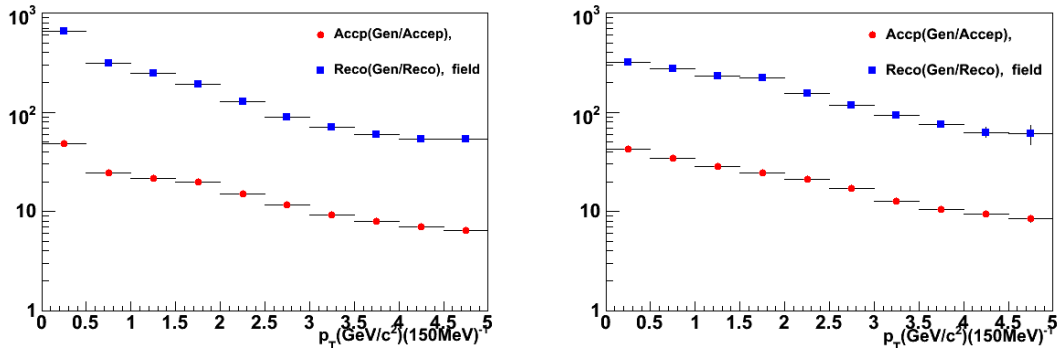

Figure 24: Correction function for ω (left) and ϕ (right).

$$\varepsilon^i = \varepsilon^i_{e^+} \cdot \varepsilon^i_{e^-}, \tag{10}$$

where

$$\varepsilon^i_{e^+} = \frac{(N_{e^+}/N_{evt})_i}{(N_{e^+}/N_{evt})_{ref.run}}, \varepsilon^i_{e^-} = \frac{(N_{e^-}/N_{evt})_i}{(N_{e^-}/N_{evt})_{ref.run}} \tag{11}$$

The final RBR efficiency is then calculated as the weighted average of the efficiencies in each run i and is shown in Fig. 25

$$\varepsilon_{RBR} = \frac{\sum \varepsilon^i \cdot N^i_{evt}}{\sum N^i_{evt}} \tag{12}$$

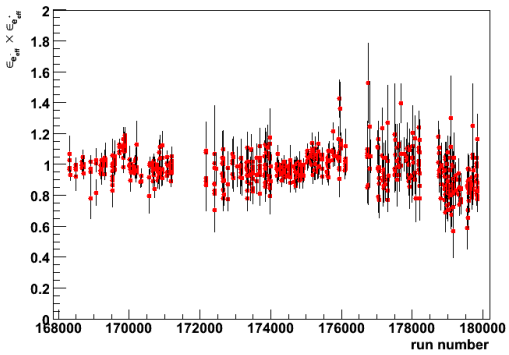

Figure 25: Run-by-run efficiency

5 Results

The main aim of this analysis is to measure the production of ϕ and ω mesons in $p+p$ and $d+Au$ collisions using di-electron decay mode. This includes the measurement of absolute differential cross-section ($\frac{1}{2\pi p_T}\frac{d^2N}{dp_T dy}$) and rapidity density (dN/dy). The dN/dy is extracted from the fully corrected invariant p_T or m_T distribution. The corrected and absolutely normalized invariant yield of ϕ or ω meson is given by:

$$\frac{1}{2\pi p_T}\frac{d^2N}{dp_T dy} = \frac{1}{2\pi p_T \cdot N_{events} \cdot BR \cdot \Delta p_T} \cdot \frac{N^{\phi,\omega}_{raw}(p_T) \cdot CF(MB)}{\varepsilon_{ERT} \cdot \varepsilon_{RBR}} \cdot \frac{\varepsilon_{BBC}}{\varepsilon_{Bias}} \tag{13}$$

where

- N_{events} is the total number of MB events corresponding to the ERT sample analyzed.

- Δp_T is the p_T bin width.
- BR is the branching ratio into e^+e^-, $7.18 \pm 0.12) \times 10^{-5}$ for ω and $2.97 \pm 0.04 \times 10^{-4}$ for ϕ.
- $CF(MB)$ is the correction factor from the simulations that takes into account the acceptance and reconstruction efficiency as obtained in Section 4.
- ε_{ERT} is the trigger efficiency as obtained in Section 4.3.
- ε_{RBR} is the run by run efficiency as obtained in Section 4.5.
- ε_{Bias} =0.79 $\pm$ 0.02, is the minimum bias trigger efficiency for $p+p$ (Sec. 2.6).
- ε_{BBC} =0.545 $\pm$ 0.06, is the BBC efficiency (Sec. 2.6).

In case of $d+Au$ collisions, the same formula is used with the following parameters.

- ε_{Bias} =0.94 $\pm$ 0.02, is the minimum bias trigger efficiency for $d+Au$ (Sec. 2.6).
- ε_{BBC} =0.88 $\pm$ 0.004, is the BBC efficiency (Sec. 2.6).

This invariant yield can be converted into an invariant cross-section by multiplying with the inelastic cross-section σ^{inel} = 42.2 $\pm$ 1.9 (2260 $\pm$ 100) mb for $p+p$ ($d+Au$) collisions.

$$E \cdot \frac{d^3\sigma}{dp^3} = \frac{1}{2\pi p_T} \frac{d^2N}{dp_T dy} \sigma^{inel} \tag{14}$$

6 Systematic Uncertainties

The present section summarizes the various sources of systematic uncertainties that contribute to the invariant spectra and cross-section determination and are summarized in Table. 8 for the ω and Table. 9 for the ϕ. In most cases, the systematic errors on the invariant spectra were estimated by varying the parameters, recalculating the invariant cross-section and monitoring their deviations from the measured value. The RMS of the variation is assigned as systematic error. The main sources of systematic uncertainties are:

Background Shape The raw yield extraction in this analysis was done using a fitting procedure. There is a systematic uncertainty due to the fact that the background shape under and around the peak is not known precisely. To extract the systematic errors due to this, the peaks were fitted with a RBW or Gaussian + n^{th} order polynomial (n = 0, 1, 2) to allow for the underlying background. The effect of varying the fitting range was also

studied. For each case, the invariant yield was recalculated and the spread of the points was assigned as the systematic error.

ERT efficiency The systematic uncertainty on the ERT efficiency was evaluated by varying the parameters of the single electron efficiency curves for each EMCal sector, by $\pm 1\sigma$ and repeating the analysis for the new ERT efficiencies. The RMS of the variation is taken as the error.

Electron identification To determine the error on electron identification, each eID cut used in this analysis (*n0, dep, emcsdφ and emcsdz*) was varied one at a time for both data and MC, keeping the others fixed to the values used in the analysis. The resulting spread of the distributions of the points was assigned as systematic error.

Run-by-run uncertainty This error was estimated by the number of e^+e^- pairs per event with standard eID cuts from the MB data sample. The RMS of this distribution was taken as the error for run-by-run efficiency.

Monte Carlo Simulation The main sources of the systematic uncertainties in the simulation are the fiducial mismatch between data and Monte Carlo. This was evaluated by comparing the number of electrons that fall into the acceptance in data to the number of electrons in MC. Fig 26 shows the comparison between the DC z and φ between data and simulation. In these figures, the MC was normalized to the data in a small two-dimensional $\varphi - z$ window where there are no dead areas. The variation of the data to the MC ratios for different windows used for the normalization gives an estimation of the systematic error.

Summary of systematic errors The total systematic errors were determined by the quadratic sum of the individual contributions. Table 8 and Table 9 summarize the various systematic errors for ω and ϕ respectively.

6.1 Transverse momentum spectra and yields

$\phi \rightarrow e^+e^-$ in $p+p$ collisions The invariant p_T spectra of ω and ϕ mesons is shown in Fig. 28 and 29. The invariant cross-section dσ/dy, was extracted by summing up values in all the bins as shown in Fig. 27 and are summarized in the Table. 10. The dN/dy values are obtained by dividing dσ/dy with inelastic $p+p$ cross-section σ_{pp}^{inel} = 42.2 (2260) mb for $p+p$ ($d+Au$) collisions.

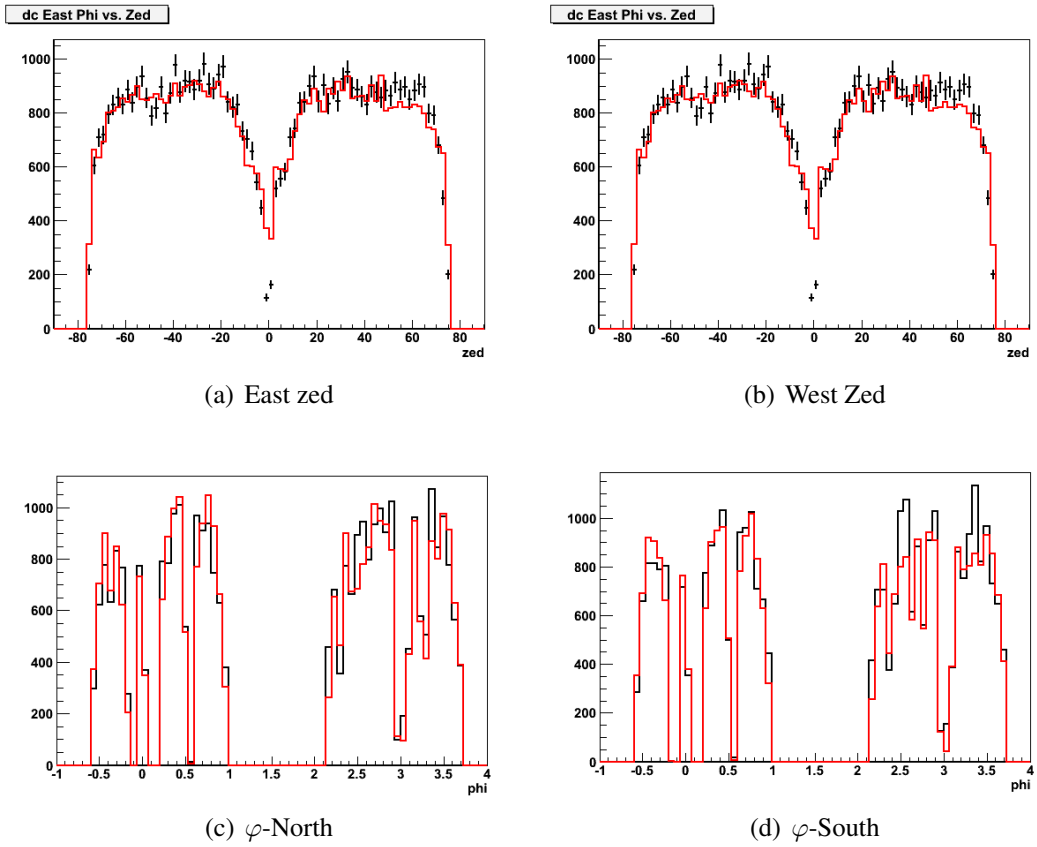

(a) East zed (b) West Zed

(c) φ-North (d) φ-South

Figure 26: The top two panels show fiducial comparison between MC and data for DC(z) for east and west arm and the bottom two panels represents the same for DC(φ).

p_T bin	0-0.25	0.25-0.5	0.5-0.75	0.75-1	1-1.25	1.25-1.5	1.5-2	2-3	3-4
Bkg. Shape	19.2	5.2	6.4	4.8	2.1	3.0	4.0	9.2	4.5
ert eff	2.4	2.4	2.3	2.0	1.8	1.6	1.3	1.0	0.9
eID	10%								
Fiducials	5%								
RBR	5%								
BR	1.7%								
$\sqrt{(\delta_{\epsilon_{bias}}2 + \delta_{\sigma_{BBC}}2)}$	9.9%								
Total	25.0	16.9	17.3	16.7	16.1	16.2	16.4	18.4	16.5

Table 8: Summary of the systematic errors for ω in $p+p$

$\phi \rightarrow e^+e^-$ **in** $d+Au$ **collisions** The invariant cross-sections of ω and ϕ mesons in $d+Au$ collisions can be seen in Figs. 30 and 31 respectively, shown together with the corresponding hadronic decay channels and $p+p$ results.

p_T bin	0-0.25	0.25-0.5	0.5-0.75	0.75-1	1-1.25	1.25-1.5	1.5-2	2-3	3-4
Bkg shape	4.4	3.8	3.1	2.9	7.0	1.0	4.2	1.0	2.0
ert eff	0.7	0.5	0.4	0.4	0.4	0.5	0.7	1.2	1.7
eID	9%								
Fiducials	5%								
RBR	5%								
BR	1.3%								
$\sqrt{(\delta_{\epsilon_{bias}}2 + \delta_{\sigma_{BBC}}2)}$	9.9%								
Total	15.8	15.7	15.5	15.5	16.7	15.3	15.8	15.3	15.4

Table 9: Summary of the systematic errors for ϕ in p+p

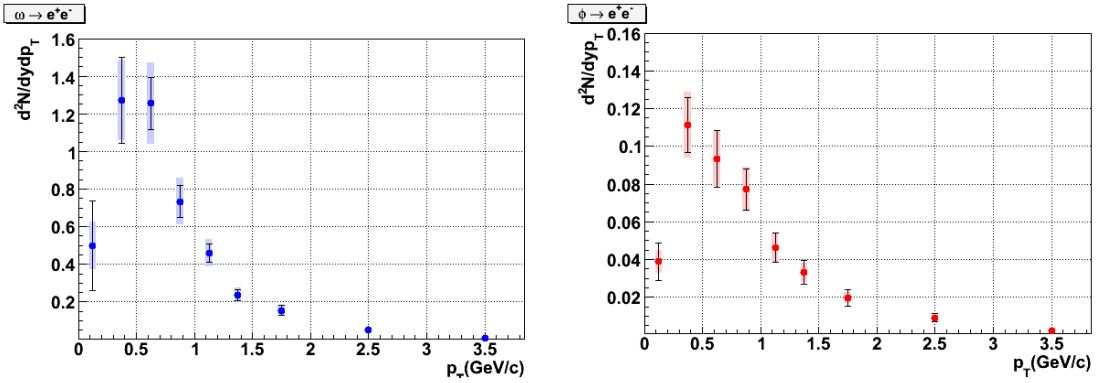

Figure 27: The left panel shows the corrected yields for ω and the right panel shows the same for ϕ

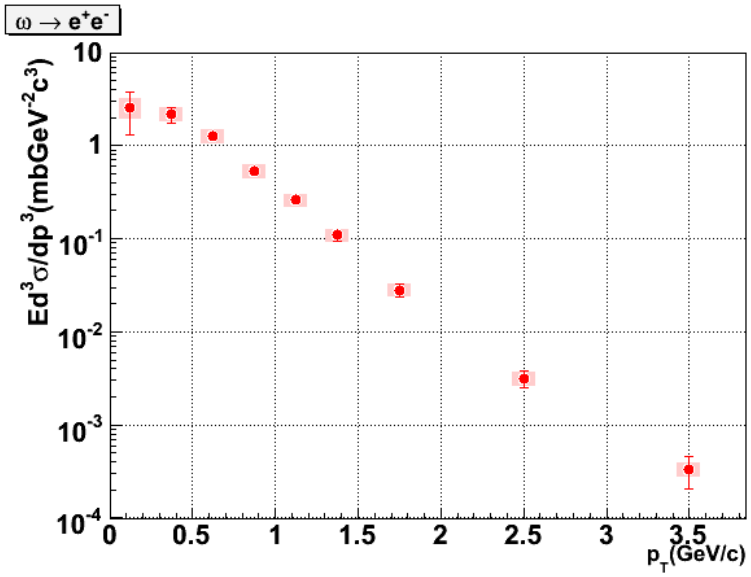

Figure 28: Invariant cross-section of ω in $p + p$ collisions as a function of p_T. The statistical errors are shown as error bars and systematic errors are shown as light red boxes.

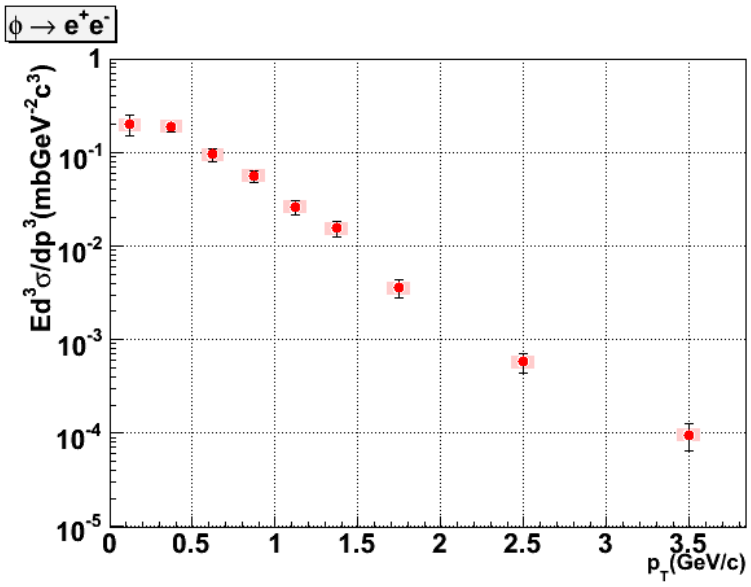

Figure 29: Invariant cross-section of ϕ in p+p collisions as a function of p_T. The statistical errors are shown as error bars and systematic errors are shown as light red boxes.

	$d\sigma/dy(\Sigma p_T$ bins)	dN/dy(Σp_T) bins
ω	4.67 $\pm$ 0.81(stat) $\pm$ 0.83(sys)	0.111 $\pm$ 0.019(stat) $\pm$ 0.019
ϕ	0.43 $\pm$ 0.07(stat) $\pm$ 0.05(sys)	0.0102 $\pm$ 0.00166(stat) $\pm$ 0.00118(sys)

Table 10: $d\sigma/dy$- values for ω and ϕ -meson extracted by integrating the p_T spectra.

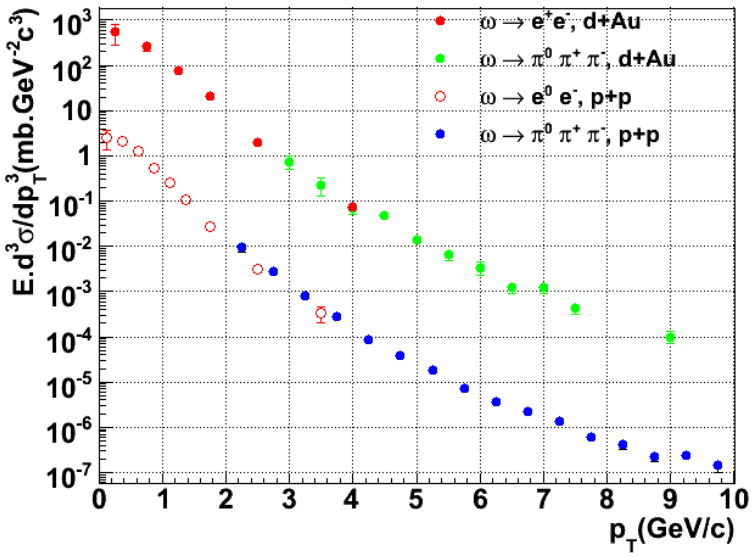

Figure 30: Invariant cross-section of ω in $d + Au$ collisions as a function of p_T overlaid with $p + p$ results. The errors shown are statistical only

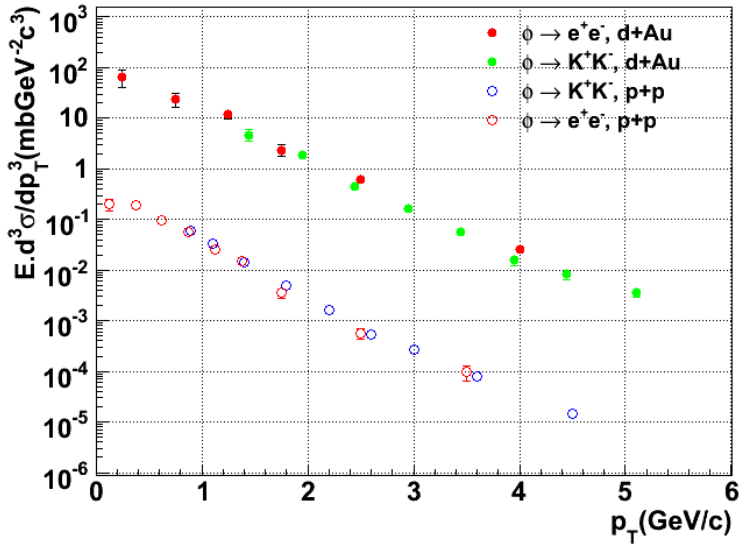

Figure 31: Invariant cross-section of ϕ in $d + Au$ collisions as a function of p_T overlaid with $p + p$ results. The errors shown are statistical only

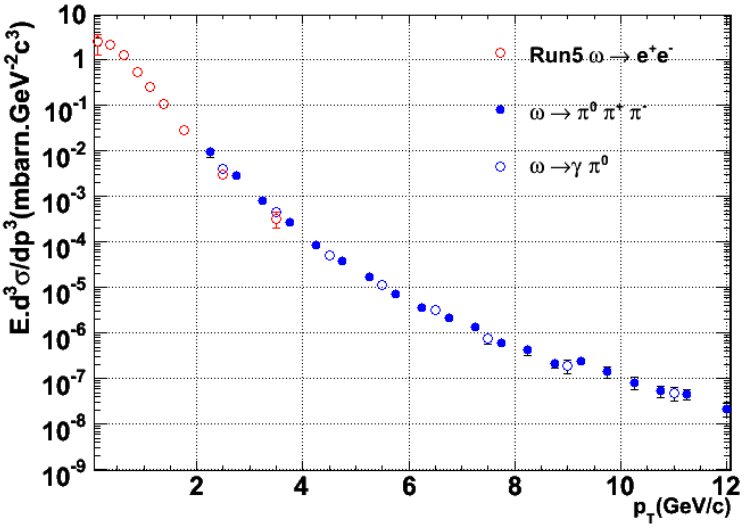

Figure 32: Invariant cross-section of ω in $p + p$ collisions as a function of p_T measured in electromagnetic and hadronic channels.

7 Summary

The in-medium resonance decays of the vector mesons ω and ϕ provide information about the hadronic phases of the medium created in heavy-ion collisions at the time of decay. To measure potential medium-modifications to the line shapes of the resonances, a baseline measurements of the line shapes in $p+p$ and $d+Au$ collisions is crucial and this analysis provides this important measurement via the e^+e^- decay channel. Shown in the Figs. 32

and 33 is the comparison of the p_T distributions in $\omega,\ \phi \rightarrow e^+e^-$ and the other measurements performed by PHENIX of the $\omega,\ \phi$ mesons via hadronic decay channels. In the region where the electromagentic and hadronic measurements overlap, a good agreement is observed.

The measurements of ω and ϕ mesons in $p+p$ collisions fit pretty well into the systematics of other mesons measured within PHENIX. This can be seen in Fig. 34 that shows a compilation of light meson measurements in PHENIX using Run3 and Run5 data and in several decay channels. The lines in the Fig. 34 are the parametrizations based on the m_T scaling to a Hagedorn function fit to charged and neutral pions data and describes the other mesons pretty well. This leads to the conclusion that in $p + p$ collisions the meson spectra are essentially driven by the mass of the particle $i.e.$ all the mesons can be described by the m_T-scaling parameterization of the π^0 spectra.

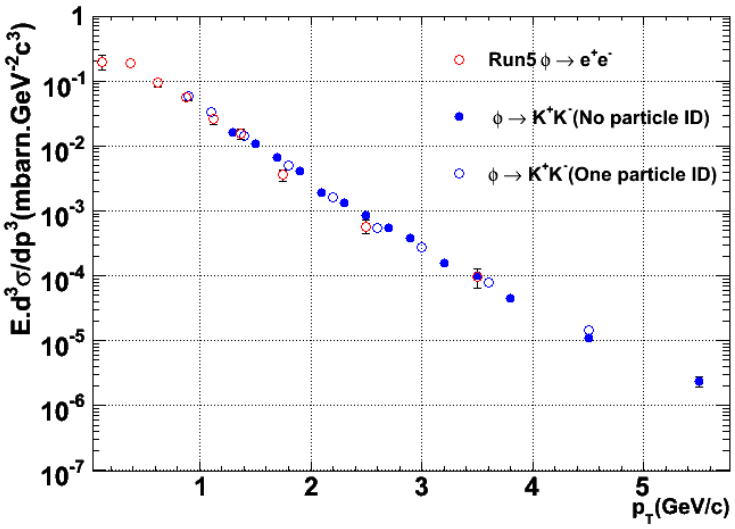

Figure 33: Invariant cross-section of ϕ in $p + p$ collisions as a function of p_T measured in electromagnetic and hadronic channels.

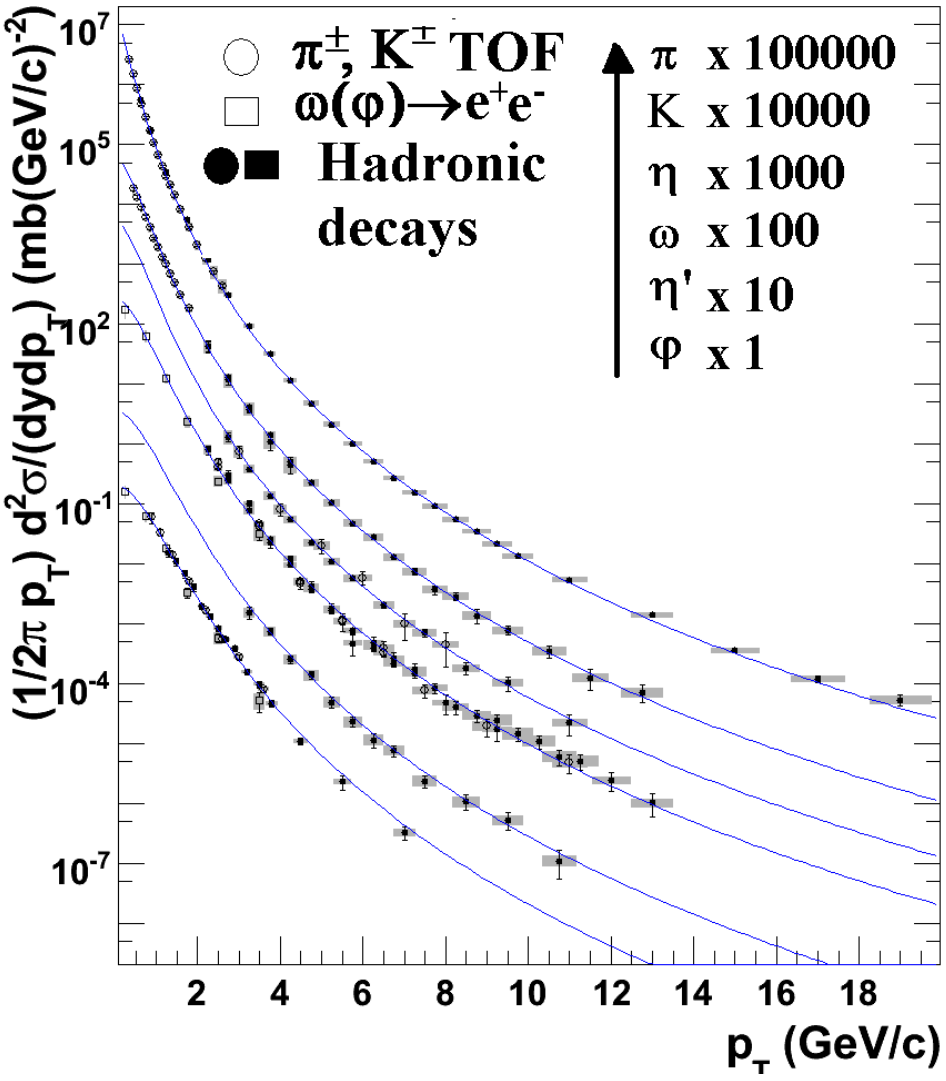

Figure 34: Compilation of PHENIX results on meson production in $p + p$ collisions at $\sqrt{s_{NN}}$ = 200 GEV. The solid lines are just to guide the eye. The data were measured using Run3 and Run5 event samples and in different decay channels.

8 Hadron Blind Detector

PHENIX has developed a novel Hadron Blind Detector[22] as an upgrade to improve the low mass dilepton measurement. The HBD will recognize and reject the tracks originating from the π^0-Dalitz decays and the γ-conversions, by using the fact that the opening angle of electron pairs from these sources is very small compared to the pairs of heavier masses. In a field-free region, this angle is preserved and by applying an opening angle cut, one can reject more than 90% of the conversions and π^0-Dalitz decays, while preserving most of the signal. The inner coil in the central arms of the PHENIX operated in the "+ -" field configuration counteracts the main field of the outer coils creating an almost field-free region close to the vertex and extending up to ∼50-60cm in the radial direction. The

HBD is located in this field-free region and hence its size is constrained by this available field-free region.

8.1 HBD Design and Construction

The Hadron Blind Detector is a windowless $\check{C}$erenkov detector with a 50 cm long radiator operated with pure CF_4, in a proximity focus configuration. A triple GEM detector element [23] avalanches the photoelectrons produced in a 350 nm *CsI* photocathode, which is evaporated on the topmost *Au* plated GEM surface and produce a blob on the pad readout plane. The use of CF_4 as a radiator and detector gas in a windowless geometry results in a very broad bandwidth (from 6 to 11.5 eV) and a very large figure of merit ($N_0 \sim 840 cm^{-1}$).

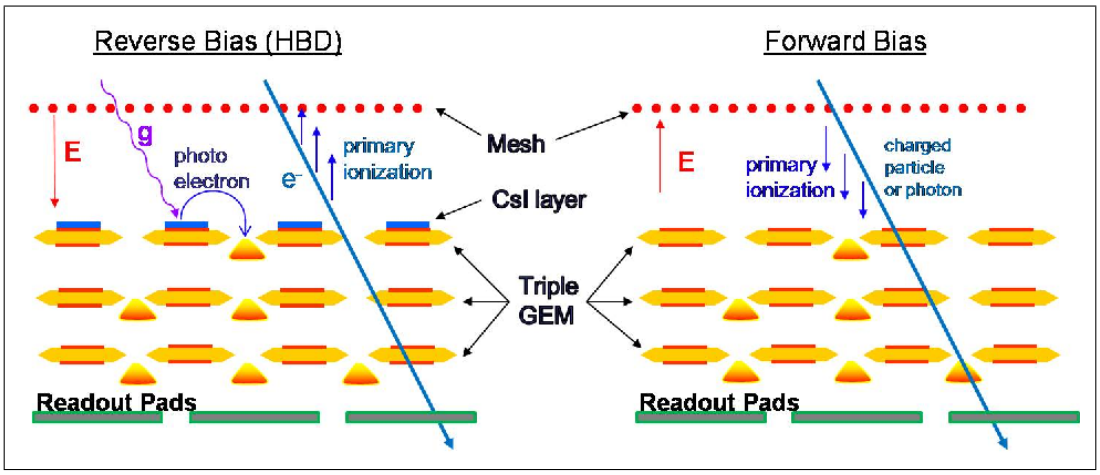

Figure 35: Gem operation modes: Left panel (FB) and Right panel (RB)

Fig. 35 shows the configuration of the triple GEM detector in the two different modes in which it can be operated. A bias voltage is applied between the top GEM and the mesh. Depending on the direction of the bias field, charge produced by ionizing particles in the upper gap can either be collected by the GEM (FB = Forward Bias)(right panel), or by the mesh (RB = Reverse Bias)(left panel). In either configuration, photoelectrons produced on the photocathode are collected with good efficiency into the GEM due to the strong electric field near the holes. In the RB mode, only a very small amount of ionization charge produced very near the photocathode (within ~ 150 μm) is collected by the GEM. The FB mode is therefore sensitive to hadrons and other charged particles, while the RB mode is essentially sensitive only to the $\check{C}$erenkov light produced by electrons and hence the term "Hadron Blind". A comprehensive R&D program was carried out to demonstrate the concept validity including studies in the lab and also a beam test at KEK. The results are published in the two NIM papers [24, 25].

8.1.1 Construction of the HBD

The design and construction of the detector vessel as well as assembly and preliminary test of the GEM foils were carried out at the WIS whereas CsI evaporation, final assembly and test of detector modules were done at the Stony Brook University. The analog and digital electronics were developed and built by BNL Instrumentation and Columbia University.

Vessel Construction The HBD consists of two identical vessels. An exploded view of one vessel with one side panel removed for clarity can be seen in Fig. 36. Each vessel has a polygonal shape and is made up of 10 panels glued together. Two FR4 frames 7 mm thick, provide mechanical stability and rigidity to the structure. The two side covers are attached to the vessel frames with plastic screws and an O-ring seal. The panels are made up of 19 mm thick honeycomb core, glued on each side to a 0.25 mm thick FR4 sheet. The side covers have a similar structure but use a 13 mm thick honeycomb core. The entrance window to the detector is a 127 μm thick mylar foil coated with 100 nm aluminum and is placed between two FR4 supports bolted to each other with an O-ring seal.

Each of the six active back panels is equipped with two triple GEM photon detectors on the inside and to the Front End Electronics on the outer side. The two panels outside the active area are used for detector services such as gas in/out, high voltage boxes and UV transparent windows. The detector anode is a double-sided printed circuit board (PCB) made of a 50 μm thick Kapton foil in one single piece (140 $\times$ 63 cm^2) and has 1152 hexagonal pads on the inner side and short (1.5 cm long) signal traces on the outer side, connected to the pads by plated through holes in the PCB. Making the PCB as one single piece and gluing it to the panels provide a good seal at the junctions between the panels. The various operations like gluing, assembling the panels etc were done with specially designed jigs and tools. The vessel construction involved $\sim$350 gluing operations per box.

Special care was taken in the design to minimize the dead areas, multiple scattering and conversions within the central arm acceptance. Each box weighs $\sim$5 Kg. Adding all accessories, HV connectors, gas in/out, GEM foils, preamplifier cards etc, results in a total weight of less than 10 Kg. The HBD contributes a total radiation length of about 3.14%, inside the central arm acceptance out of which 0.919% comes from vessel, 1.88% from the electronics installed on the back of vessel and 0.54% from the 50 cm long CF_4 radiator.

It is extremely important to have a leak-tight detector. Both water and oxygen have absorption bands in the deep UV region that absorb $\check{C}$erenkov light and reduce the overall photoelectron yield. Every 10 ppm of either oxygen or water result in a loss of approx-

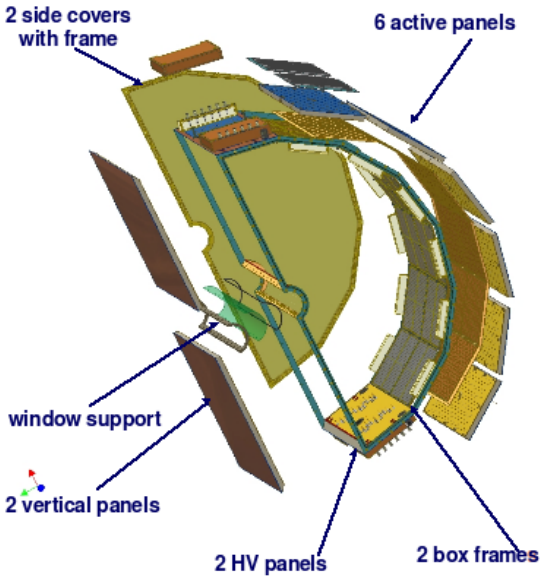

Figure 36: A 3-d view of the HBD final design.

imately 1 photoelectron due to absorption in a 50 cm long CF_4 radiator. The water also adversely affects the photocathode performance, reducing its quantum efficiency. The leak-rate in each one of the 311 litres vessel was measured to be < 0.12cc/min.

Assembly and Testing of GEM foils The HBD consists of 24 identical detector modules, 12 in each arm, 6 along $\varphi\times$ 2 along z, each one with a size of 23 $\times$ 27 cm^2. Each detector module is comprised of a 90% transparent stainless steel mesh and three GEM detectors. A standard GEM foil is a thin (50 μm) Cu-clad (5 μm) kapton foil perforated with holes of 80 μm diameter at a pitch of 150 μm. The top GEM facing the detector volume has a 0.2-0.4 μm layer of CsI evaporated on its surface previously coated with thin Gold and Nickel layers. The Gold layer prevents chemical reaction of the CsI with the copper of the GEM and the Ni acts as an adhesive agent between gold and copper. One surface of the GEM foil is divided into 28 HV segments to reduce the capacitance and stored energy in case of discharge. The entrance mesh and the three GEM foils are mounted on FR4 fiberglass frames. The frames have a width of 5 mm and a thickness of 1.5 mm that defines the inter-gap distance. They also have a supporting cross shape (0.3 mm thick in the middle), which prevents sagitta of the foils in the electrostatic field. The three GEM foils and mesh are stacked together and attached to the detector vessel by 8 pins, located at the corners and middle of the frames, that maintain the tension and prevent deformation of the 5 mm wide frames. The design allowed for only 1 mm clearance between two adjacent detectors. With this design, the resulting total dead area within the central arm acceptance is calculated to be 6%.

The different operations like gluing, stretching and high voltage testing of the GEM foils was done either in a clean room or in a stainless steel box. The GEM foil was first stretched on a special stretching device and while stretched, glued onto the FR4 frames using epoxy. Once the epoxy was cured, the GEM foil was cut from the stretching device and SMD resistors were soldered across each HV segment. The GEMs were monitored for leakage current and discharges at every step namely before framing, after gluing and after soldering the resistors. A good GEM was required to draw current below 5 nA. A GEM that passed all these quality control tests was then mounted inside a stainless steel vessel and was tested up to 520V in CF_4. It was then mapped for gain variations in Ar/CO_2 using a collimated ^{55}Fe source, positioned inside the box. The measured gain values (corrected for pressure and temperature variation) were then stored in the PHENIX database.

Due to small differences in the hole diameters, the GEMs have local gain variations that lead to an additive effect in the triple GEM assembly. A random combination of GEMs for the triple GEM assembly thus led to local gain variations which could be as high as 50%. In order to have the lowest possible gain variations in all modules, gain maps of the single GEMs were used to determine all possible triplets combinations and the best ones leading to the smallest gain variations were selected. The resulting gain spread for module to module varied from 5% to 20% in all the 24 modules. Fig. 37 shows the measured gain uniformity of an installed stack in the HBD selected using this strategy. Out of a total of 65 standard and 47 gold plated GEMs that passed all the quality assurance tests, 48 standard and 24 Gold GEMs were used to construct the final detector.

Readout electronics Circuit boards containing the readout electronics were installed on the back side of the vessel. The readout board is a multilayer board which contains the preamps and has a signal layer that drives the differential output signals from the preamps to connectors located at the edge of the board. The preamps used are hybrid preamplifiers, the $IO1195-1$, developed by the Instrumentation Division at BNL. The gain is set to give an output signal of $\pm$50 mV for an input signal of 16fC (100,000 e's), corresponding to an average signal of 20 photoelectrons per pad at a gas gain of 5×10^3. The preamp signals are digitized using a flash ADC.

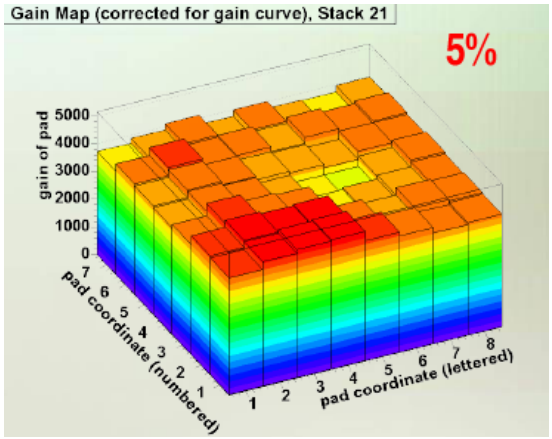

Figure 37: Gain map of one of the triple GEM stacks presently installed in the HBD

8.2 HBD Commissioning

A full scale prototype of the HBD with only one instrumented sector was installed in PHENIX during the $p+p$ physics run in 2006. The prototype data analysis demonstrated the basic properties of the HBD $i.e.$ hadron blindness and electron hadron separation. This is shown in Fig. 38. The left panel shows the cluster amplitude distribution for minimum ionizing particles obtained in FB (blue) and RB (red) configurations. The FB spectrum is nicely fitted with a Landau distribution, a prominent feature of the energy loss of a minimum ionizing particle (mip). The RB spectrum on the other hand clearly shows a strong suppression of the direct ionization signal, as expected. The right panel shows the same distribution in the RB mode compared to the distribution of electrons identified by the PHENIX central arm detectors. The signal from minimum ionizing particles is significantly lower compared to that from electrons demonstrating the electron hadron separation.

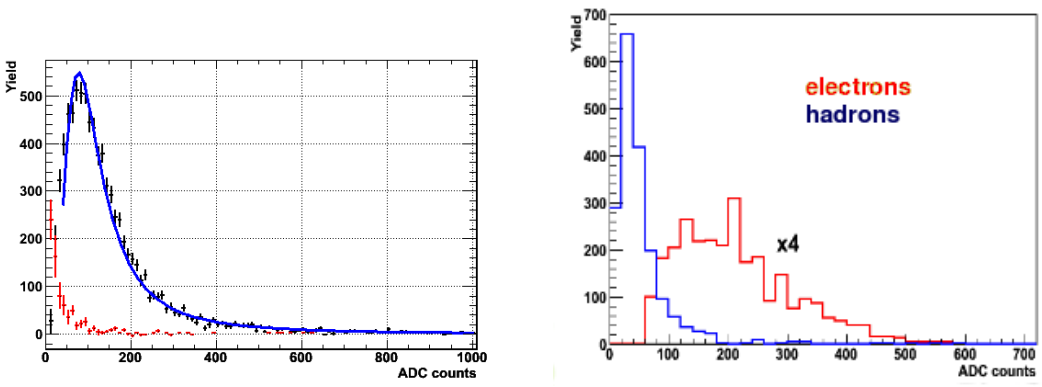

(a) (b)

Figure 38: Cluster amplitude (a) measured with the forward voltage bias (blue) and reverse bias in red. (b) Same for identified hadrons (blue) and electrons (red) in reverse bias mode.

A commissioning run of the HBD took place in the 2007 $Au+Au$ RHIC run (Run7). The detector showed problems in holding high voltage. Due to an inherent flaw in the LeCroy firmware, the mesh voltage was momentarily reapplied 200 ms after a trip, leading to a large potential difference in the 1.5 mm gap between the mesh and the top GEM, resulting in sparks. Many times the UV light from a single discharge would induce discharges on other GEM stacks in the line of sight, making several stacks to trip simultaneously. These massive discharges produced irreparable damage to several GEMs. The problem with the high voltage hardware was fixed during the run by installing zener diodes between the mesh and top GEM to remove the possibility of large voltage differences. These fixes prevented the massive trips and the detector operated rather stably

for the rest period of the run. Later when the detector was dismantled, it was clear that the reasons for sparks in the GEMs was trapped dust inside the detector. The detector has been refurbished and extreme care was taken to maintain a clean environment during the assembling of the GEMs. The detector is now integrated into PHENIX and the initial tests show no problems with the GEMs holding high voltage, as was seen in the previous year.

8.3 Gain determination

One of the basic requirements of the HBD is to have an excellent ability to differentiate between single and double electrons. The signal amplitude from GEMs should produce well separated peaks for single and merged hits. The variations in gain across the detector and over time can lead to a smearing of the spectra and hence no clear separation between single and double hits. It is therefore crucial to measure the absolute gain of each module and equilibrate the whole detector and also over time. During the analysis of run7 data, we devised a new scheme for the gain determination. The method exploits the scintillation hits produced by the gas inside HBD. By measuring the scintillation spectra, one can determine gain as described below:

We first select scintillation hits, identified as single fired pads that do not have any central arm track associated to them. Since the central collisions have a high occupancy, we select peripheral events for this. The spectra thus obtained are shown in the top panel of the Fig. 39 for one HBD module, EN3 (EN3 means the module located in east arm, north side and in sector 3), for both the FB and RB configurations. In the FB case, one can clearly see two components, one is a fast exponential and the other is a slow exponential. The fast component survives completely in the RB mode as seen in the lower panel and this corresponds to the scintillation hits. This lower part is then fitted to an exponential function.

$$y = p_0 \cdot exp(p_1 \cdot x) \tag{15}$$

The gain is then given by

$$Gain = \frac{1/p_1(slope)}{< m >} \tag{16}$$

where $< m >$ is the average number of scintillation photons in the fired pad. To determine the value of $< m >$, we follow the assumption that number of scintillation photons per pad follows a Poisson distribution

$$P(n) = \frac{\mu^n e^{-\mu}}{n!} \tag{17}$$

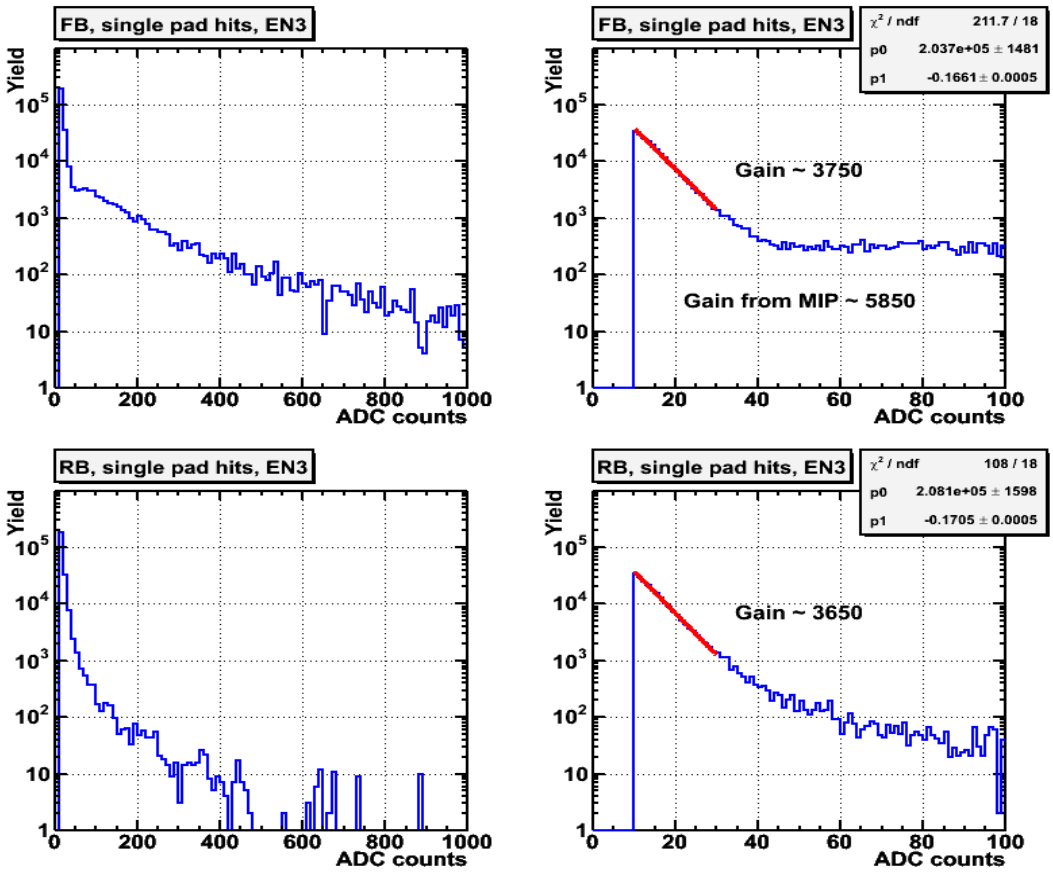

Figure 39: The upper two spectra corresponds to the FB modes (the right one is a zoom of the low amplitude region). The lower two plots represent the spectra for RB mode

where a fired pad measures on the average $< m >$ photoelectrons given by:

$$< m >= \frac{\sum_{n\geq 1}^{\infty} nP(n)}{\sum_{n\geq 1}^{\infty} P(n)} = \frac{\mu}{1 - P(0)} \tag{18}$$

where P(0) is the probability for not having a hit in the pad = $e^{-\mu}$

$$< m >= \frac{\mu}{1 - e^{-\mu}} \approx 1 + \frac{\mu}{2} = 1 - \frac{ln[P(0)]}{2} \tag{19}$$

It is not possible to measure P(0), since the signal processing algorithm has a threshold of ADC counts for noise suppression. What instead can be done is to repeat the above procedure for various thresholds to define a fired pad. The measured curve for $< m >$ as a function of pad threshold can then be extrapolated to zero to obtain P(0) as seen in Fig. 40(b). The above method was repeated for various classes of event centrality and the absolute gain determined came independent of the centrality class, demonstrating the validity of the method. The different curves for various centrality classes can be seen

in Fig. 40(b) and the corresponding uncorrected and corrected gains are shown in the Fig. 40(c).

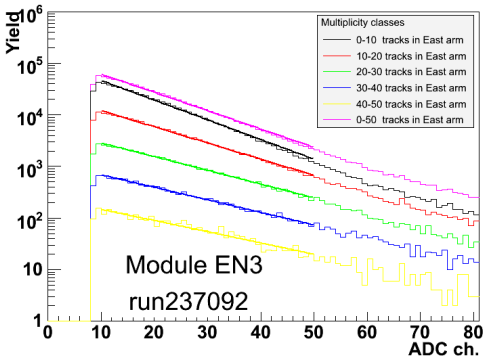

(a) ADC spectra for different number of tracks

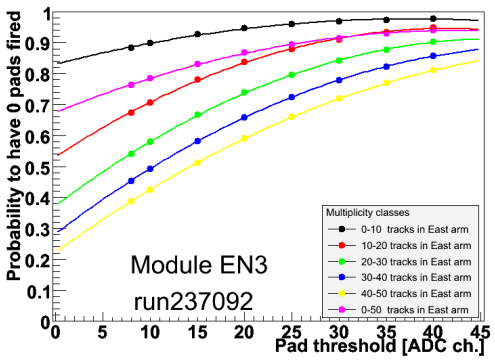

(b) extrapolation to extract P(0) values for different cases

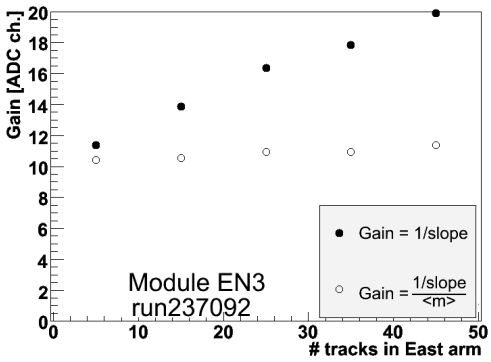

(c) Gain corrected with P(0)

Figure 40: (a) shows the ADC spectra for various event classes, based on the number of tracks. (b) shows the curves for each event class, for various pad firing thresholds to extract P(0). (c) shows the uncorrected and corrected gain extracted.

This procedure was used to derive the gain for all the active modules in Run7 data analysis. Also the gain for each individual run was determined using this method to take care of time variations.

References

[1] PHENIX detector overview K.Adcox et al., NIM A499 469-477(2003). 1

[2] K. Adcox et al. (PHENIX Collaboration), Nucl. Instr. and Meth. A499, 469 (2003). 1

[3] Z. Fraenkel, B. Khachaturov, A. Kozlov, A. Milov, D. Mukhopadhyay, D. Pal, I. Ravinovich, I. Tserruya and S. Zhou, The PHENIX Collaboration Technical Note 391, http://www.phenix.bnl.gov/phenix/WWW/publish/tserruya/1-06-HBD-proposal.ps. 1

[4] M. Adamczyk et al., Nucl. Instr. and Meth. A 499, 437 (2003). 2

[5] B.B. Back et al., Nucl. Instr. and Meth. A 499, 603 (2003). 2

[6] K.H. Ackermann et al., Nucl. Instr. and Meth. A 499, 624 (2003). 2

[7] M. Allen et al., Nucl. Instr. and Meth. A 499, 549 (2003). 2

[8] T. Ludlam, Nucl. Instr. and Meth. A 499, 428 (2003). 2

[9] C. Adler et al., Nucl. Instr. and Meth. A 470, 488 (2001). 2

[10] K. Adcox et al., Nucl. Instrum. Methods Phys. Res., Sect. A 499, 489 (2003). 5

[11] D. Ben-Tzvi, M.B. Sandler, Pattern Recognition Lett. 11 (1990) 167. 5

[12] M. Ohlsson, et al., Comp. Phys. Commun. 71 (1992) 77. 5

[13] K. Adcox et al., Nucl. Instrum. Methods Phys. Res., Sect. A 497, 263 (2003). 5

[14] The complete volume Edited by M. Harrison, T. Ludlam and S. Ozaki, Volume 499, Issues 2-3, Pages 235-880 (1 March 2003) The Relativistic Heavy Ion Collider Project: RHIC and its Detectors 7

[15] Y. Akiba et al., Nucl. Instr. and Meth. A 433, 143 (1999). 7

[16] W. M. Yao et al., Journal of Physics G 33, 1 (2006). 7

[17] S. S. Adler et al., Nucl. Instr. and Meth. A 499, 560 (2003). 8

[18] Y. Riabov (PHENIX Collaboration), Measurement of leptonic and hadronic decays of ω and ϕ mesons at RHIC by PHENIX, J. Phys. G34, S925 (2007)

[19] D. Ivanishchev, A. Milov, V. Riabov and Y. Riabov, Hadron decays of ω and K_s^0 mesoms in Run5 $p+p$ (2006), PHENIX Internal Analysis Note 535.

[20] S. S.Adler $etal.$, (PHENIX Collaboration), Production of ω mesons at large transverse moments in $p+p$ and $d+Au$ collisions at $\sqrt{s_{NN}}$ = 200 GeV, Phys. Rev. C 75, 051902 (2007).

[21] D. Ivanishchev $etal.$, $\phi \rightarrow K^+K^-$ measurement in Run5 $p+p$ and Run3 $d+AU$ with no PID (2006) PHENIX Internal Analysis Note 600.

[22] Technical Note 391: Proposal for a Hadron Blind Detector for PHENIX, 2001. 35

[23] F. Sauli, Nucl. Instr. and Meth. A523 (2004), 345 36

[24] A. Kozlov, I. Ravinovich, L. I. Shekhtman, Z. Fraenkal, M. Inzuka and I. Tserruya, Nucl. Instrum. Meth A523, 345(2004)[arXiv: physics/0309013]. 36

[25] Z. Fraenkel et al., Nucl. Instrum. Meth. A546, 466(2005) [arXiv: physics/0502008]. 36